Relationship of gravity waves and small scale variations in noctilucent clouds
observed by lidar at 69° N

Masterarbeit

am Leibniz-Institut für Atmosphärenphysik Kühlungsborn
an der Universität Rostock

von
Christine Ridder

Gutachter: Prof. Dr. Franz-Josef Lübken, Universität Rostock
Dr. Gerd Baumgarten, IAP Kühlungsborn

Rostock, den 12. September 2014

Abstract

Noctilucent clouds (NLC) are ice clouds forming in the cold summer mesopause at high latitudes. Their structured appearance is caused by atmospheric gravity waves that create fluctuations in the background atmosphere. NLC are therefore used as a tracer for gravity waves at mesospheric heights, a region difficult to study otherwise. In the years 2009–2013, vertical NLC brightness profiles were measured with the Rayleigh/Mie/Raman lidar at ALOMAR in Norway, 69° N, during almost 1000 h at a high temporal and spatial resolution (30 s $\times$ 40 m). In this thesis, a pattern recognition algorithm is developed to extract the altitude variations of the NLC layer on small temporal scales (5–200 min). The period is determined with a Lomb-Scargle frequency analysis and, in combination with simultaneous radar wind data, a horizontal scale of the wave patterns is calculated, that corresponds geophysically to the approximate wavelength of the gravity waves. The variations show a high occurrence of periods of 5–20 min and of horizontal wavelengths of 10–30 km, which is consistent with camera observations of NLC, which are limited to twilight conditions, and of airglow. The propagation properties of the gravity waves are analyzed using the duration of the wave events, showing the appearance of a few single events extending over many wave cycles.

Zusammenfassung

Leuchtende Nachtwolken (NLC) sind Eiswolken, die sich in der kalten Sommermesopause in hohen Breiten bilden. Ihre strukturierte Erscheinung entsteht durch atmosphärische Schwerewellen, die Schwankungen in der Hintergrundatmosphäre verursachen. NLC werden daher als Tracer für Schwerewellen in mesosphärischen Höhen genutzt, eine Region die ansonsten schwierig zu untersuchen ist. In den Jahren 2009–2013 wurden während fast 1000 h vertikale Helligkeitsprofile von NLC mit dem Rayleigh/Mie/Raman-Lidar in ALOMAR in Norwegen (69° N) mit hoher zeitlicher und räumlicher Auflösung (30 s $\times$ 40 m) gemessen. In dieser Arbeit wurde eine Mustererkennung entwickelt um die zeitlich kleinskaligen (5–200 min) Höhenvariationen der NLC-Schicht zu extrahieren. Die Periode wird mittels einer Lomb-Scargle-Frequenzanalyse bestimmt. Kombiniert mit gleichzeitigen Winddaten von Radarmessungen wurde eine horizontale Skala der Wellenmuster berechnet, die geophysikalisch einer Näherung der Wellenlänge der Schwerewellen entspricht. Die Variationen treten verstärkt mit Perioden von 5–20 min und horizontalen Wellenlängen von 10–30 km auf, was mit Messungen von Kamerabeobachtungen von NLC, welche jedoch auf Messungen bei Dämmerung beschränkt sind, und von Airglow übereinstimmt. Die Ausbreitungseigenschaften von Schwerewellen wurden mittels der Dauer der einzelnen Wellenereignisse untersucht, die einzelne Ereignisse zeigen, welche sich über viele Wellenzyklen ausdehnen.

Contents

1 Introduction **9**

2 Theoretical background **11**
2.1 Atmosphere 11
2.2 Gravity Waves 12
2.3 Noctilucent clouds 14

3 Instruments **19**
3.1 Rayleigh/Mie/Raman lidar 19
3.2 Saura MF radar 22

4 Data analysis **23**
4.1 Motivation 23
4.2 Preprocessing 25
4.3 Pattern recognition 25
4.4 Wave patterns 30
4.5 Lomb-Scargle periodogram 31
4.6 Estimation of the horizontal wavelength 33

5 Results **35**
5.1 Limits of the analysis: synthetic NLC 36
5.2 Periods found in NLC 39
5.3 Approximate wavelengths in NLC 41
5.4 Duration of wave signatures 42

6 Discussion **45**
6.1 Limits and uncertainties 45
6.2 Comparison to other gravity wave observations in the mesopause region . . . 49
6.3 Gravity wave propagation 52

7 Conclusion and outlook **57**

1 Introduction

The atmosphere of the Earth is a complex and dynamic environment. It provides a protective layer that prevents the high-energy solar radiation from reaching the Earth's surface and keeps the radiation emitted from the ground from dissipating directly into space, creating the climatic conditions that make life on Earth possible. Small changes can disturb the fragile equilibrium of the Earth-Atmosphere system, as it is currently observed with the climate change. While the temperature at the ground is increasing slightly, the changes are more dramatic at higher altitudes, where instead of an increase, there is a ten times higher decrease in temperature. The many different parameters make the changes difficult to predict and a detailed knowledge of the processes governing the entire atmosphere more important. However, it is not only about the future development of the climate, even in the current state all the dynamics of the atmosphere are far from being completely understood.

The lower 10 km of the atmosphere are well known for all kinds of weather events, that are essentially limited to this lower layer. The atmosphere extends far higher, with an exponentially decreasing density, such that the atmosphere, compressed to the ground pressure, would be only around 8 km high. Above 10 km begins the middle atmosphere whose upper boundary at the mesopause around 90 km marks the transition into space. The study of the mesopause region is especially challenging, since this height can hardly be accessed at all for measurements. Therefore, the mesopause has for a long time been one of the least known regions of the atmosphere. By now it is known that its role in the atmosphere cannot be neglected, on the contrary, waves that are breaking at this height are driving global meridional circulation in the middle atmosphere (e.g. *Holton*, 1983).

There, at the edge of space, extreme conditions during the summer at high latitudes allow the formation of thin ice clouds, similar to the cirrus clouds in the lower atmosphere. These clouds, known as noctilucent clouds (NLC), owe their name to their spectacular appearance. Visible only when the sun is just below the horizon, they are still illuminated by the sun and seem to glow in the already dark sky. The ALOMAR observatory is located at 69° N, where NLC are observed in about 50 % of the time during the high season in mid July (*Fiedler et al.*, 2009). With sounding rockets currently being the only possibility for in situ measurements, noctilucent clouds are a valuable tracer for remote observations in this region of the atmosphere, that can be observed by many means, even by naked eye. Independently of how the clouds are observed, their most striking feature is their structure which features wave patterns at different scales.

Waves with wavelengths from a few to hundreds of kilometers propagate through the atmosphere, horizontally and vertically, and transport energy and momentum over large distances from their source to their breaking region. Gravity waves, driven by the buoyancy, propagate from the surface to the upper regions of the atmosphere. Planetary waves surround the globe with the Coriolis force as restoring force and periodic changes, like the day-night cycle, create tides. They all manifest in variations of various parameters of the atmosphere, like the temperature, the wind, or the density and thereby can also be seen in clouds. In noctilucent clouds, the waves near the mesopause are directly visible, even the small scale gravity waves, that play an important role for the meridional circulation (e.g. *Fritts and Alexander*, 2003). Models for the global circulation are working with far lower resolutions and can therefore not resolve those small scale waves. Instead, they rely on parametrizations, for which a detailed knowledge about the properties of these waves is necessary.

The methods of observations of the atmosphere are vast, but only a few of them can be used for the mesopause region. At latitudes where the sun is low enough in the summer, ground based camera images of noctilucent clouds are valuable observations (e.g. *Witt*, 1962). Satellite measurements provide global observations, but are limited to a few measurements per day. Lidar observations are one possibility to measure locally, but at a high temporal and vertical resolution. Continuous improvement of the ALOMAR RMR lidar now allows measurements with resolutions high enough to clearly resolve the small scale variations in NLC of only a few minutes (*Kaifler et al.*, 2013).

The objective of this thesis is the systematic study of the visible small scale variations in lidar observations of NLC with the ALOMAR RMR lidar. In each measurement of NLC, wave structures in the height of the NLC layer are visible, with periods of only a few minutes. The small periods and in some cases very short wave patterns, sometimes only a single oscillation, are difficult to extract with a wavelet analysis over the entire NLC data. In previous studies using camera or satellite images, small scale wave events were identified visually and then analyzed further. However, this approach cannot be applied to a multi year data set. Only during the recent years from 2008 to 2013, after the realization of measurements with a temporal resolution of only 0.5 min, over 1000 h of measurements containing NLC were obtained, thanks to measurement campaigns every summer.

As a solution, a pattern recognition algorithm was developed, that identifies the single wave events in the NLC data, whose period can then be determined, as well as the corresponding wavelength based on the wind. The extraction of the waves in NLC offers many further information beside the wavelength, including the length of the individual wave events, their amplitude, their occurrence rate and the presence of multiple layers.

In Chapter 2, a theoretical overview of the atmosphere, gravity waves, and noctilucent clouds is given. The instruments used for the data acquisition, the ALOMAR RMR lidar and the Saura MF radar, are described in Chapter 3. The processing of the data, the pattern recognition, and the computation of the period and the wavelength is explained in Chapter 4, followed by the results in Chapter 5 and their discussion, comparison to similar studies, and the geophysical context in Chapter 6. Chapter 7 summarizes the results and presents an outlook for further studies.

2 Theoretical background

2.1 Atmosphere

The atmosphere is a stratified fluid, with the air near the surface having a higher density due to the pressure exerted by the air above in the gravity field of the Earth. The pressure p at an altitude z is given by the hydrostatic equation, which describes the balance between the pressure and the weight of the overlying air column

$$dp = -\rho g \, dz, \tag{2.1}$$

with the density ρ and the gravitational acceleration g. The hydrostatic approximation applies where the vertical acceleration is small compared to g, a condition that is well fulfilled in the atmosphere. With the further assumption that the atmosphere behaves as an ideal gas, such that

$$p = nkT, \tag{2.2}$$

where n is the number density, k the Boltzmann constant and T the temperature, the vertical profile of the atmospheric pressure can be derived from the hydrostatic balance as

$$p(z) = p(z_0) \exp\left(- \int_{z_0}^{z} \frac{mg}{kT(z')} \, dz' \right). \tag{2.3}$$

For an isothermal atmosphere, this simplifies to

$$p(z) = p(z_0) \, e^{-\frac{z-z_0}{H}} \tag{2.4}$$

where the scale height

$$H = \frac{kT}{mg} \simeq 8\,\mathrm{km} \tag{2.5}$$

defines the height at which the pressure has decreased by a factor of e. This exponential decrease implies that 99 % of the mass of the atmosphere are in the lower 32 km. Despite its small share in mass, the remaining higher atmosphere and its role in global processes cannot be neglected.

Depending on the temperature gradient, the atmosphere is divided into different layers. Reference temperature profiles of the atmosphere with the corresponding layers are shown in Figure 2.1. In the lowest layer, the troposphere, most weather phenomena take place. The incoming solar short-wave radiation is absorbed by the Earth's surface and the energy is re-emitted in form of long-wave radiation. The atmosphere is heated through the surface and cools down with increasing height up to the tropopause at a height of 10 km at high latitudes and 15 km near the equator.

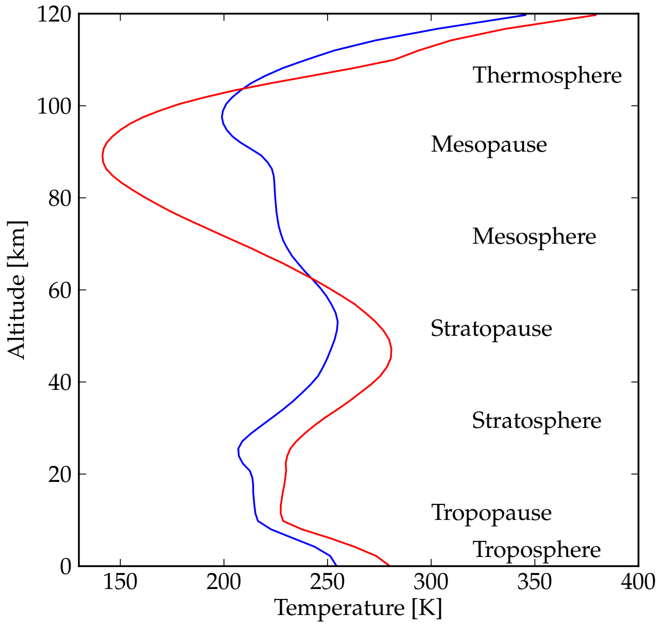

Figure 2.1: Atmospheric temperature profile at 70° N in January (blue) and July (red) from the CIRA-86 reference atmosphere (*Fleming et al.*, 1990) with the atmospheric layers and boundaries.

The increase of the ozone in the atmosphere becomes notable in the stratosphere. The ultraviolet radiation from the sun is absorbed by the ozone and therefore heats the surrounding air. The increasing temperature determines the extent of the stratosphere from 10 to 50 km. Above the stratopause at 50 km, the temperature decreases again in the mesosphere. Finally, in the thermosphere above the mesopause at around 90 km, the temperature rises by absorption of high energy radiation.

The temperature profile varies between summer and winter in higher latitudes. While the lower atmosphere is warmer in summer than in winter, the mesosphere is much colder. In fact, the lowest temperatures of the atmosphere are found in the polar summer mesopause. With mean temperatures as low as 130 K (*Lübken*, 1999), the conditions are favorable for the formation of ice clouds, referred to as noctilucent clouds or NLC that will be addressed in Section 2.3. This temperature distribution is the result of the global circulation of air masses which is discussed in the following section.

2.2 Gravity Waves

Gravity waves are mechanical waves with the density difference or buoyancy as the restoring force. When an air parcel is displaced vertically in the atmosphere, its pressure adjusts to the new atmospheric background pressure. Its temperature T_{ap} then changes according to the adiabatic lapse rate Γ

$$\frac{\mathrm{d}T_{\mathrm{ap}}}{\mathrm{d}z} \simeq -\frac{g}{c_p} = \Gamma \simeq -10\,\mathrm{K\,km^{-1}} \tag{2.6}$$

with c_p the specific heat at constant pressure. If the temperature of the background atmosphere decreases faster than the adiabatic lapse rate ($^{dT}/_{dz} < \Gamma$), the density of the displaced air parcel is lower than the density of the surrounding air. The air parcel therefore continues to rise: The conditions are statically unstable. In the case of a stable atmosphere with $^{dT}/_{dz} > \Gamma$, the air parcel becomes denser than the surrounding air and tends back to its equilibrium position. The frequency of this oscillation is the Brunt-Väisälä frequency N, or buoyancy frequency

$$N^2 = \frac{g}{T}\left(\frac{\mathrm{d}T}{\mathrm{d}z} - \Gamma\right) = \frac{g}{T}\left(\frac{\mathrm{d}T}{\mathrm{d}z} + \frac{g}{c_p}\right). \tag{2.7}$$

The dispersion relation for gravity waves is given by

$$\omega_\mathrm{I}^2 = \frac{N^2\left(k^2+l^2\right) + f^2\left(m^2 + \frac{1}{4H^2}\right)}{k^2+l^2+m^2+\frac{1}{4H^2}} \tag{2.8}$$

with ω_I being the intrinsic frequency of the wave, k, l and m the horizontal and vertical wave numbers, and the Coriolis parameter $f = 2\Omega\sin\phi$, where ϕ is the latitude (*Fritts and Alexander*, 2003). Alternatively, for their vertical wavenumber m,

$$m^2 = \frac{\left(k^2+l^2\right)\left(N^2-\omega_\mathrm{I}^2\right)}{\left(\omega_\mathrm{I}^2 - f^2\right)} - \frac{1}{4H^2}. \tag{2.9}$$

From the dispersion relation it follows that propagating waves have frequencies limited by a maximum frequency of N and a minimum frequency of $|f|$. If $\omega_\mathrm{I} > N$, then $m^2 < 0$, which means that the wave is evanescent and does not propagate vertically (*Isler et al.*, 1997).

Most gravity waves are generated in the troposphere. The main sources include the topography, convection or wind shear (e.g. *Fritts and Alexander*, 2003). From there they propagate upwards in higher atmosphere layers. With the decrease of the density with height, the amplitude of the gravity wave increases, until eventually the wave becomes unstable and breaks. Until then, the wave can travel great distances due to an inclined propagation. When the background conditions like wind or temperature change, the wave can be refracted or reflected (*Pitteway and Hines*, 1965). Ray tracing models like GROGRAT describe the propagation of gravity waves through the atmosphere from the source up to the dissipation of the wave (*Eckermann and Marks*, 1997).

Gravity waves are important to middle-atmosphere dynamics by transporting momentum and energy over large distances, vertically as well as horizontally. On global scales they contribute to the temperature distribution by driving the meridional circulation. The polar summer mesopause is the coldest region of the atmosphere. It is exposed to continuous sunlight and is still about 70–80 K colder than the dark winter mesopause. This unexpected cooling far from radiative equilibrium is maintained by gravity waves (e.g. *Holton*, 1983; *Geller*, 1983; *Meriwether and Gerrard*, 2004)

The gravity waves that propagate upwards in the atmosphere are filtered by the background wind. When the wind becomes larger than the phase speed of the wave, the wave reaches a critical layer and cannot propagate further upwards. The mean wind profiles

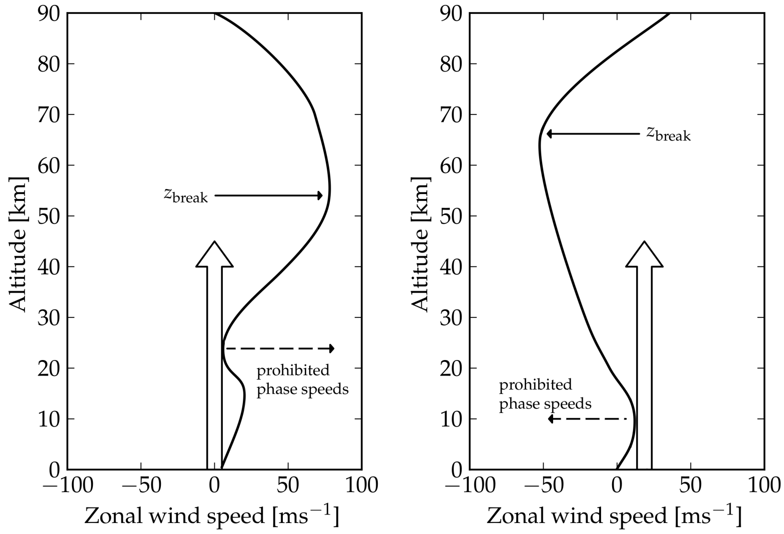

Figure 2.2: Mean zonal wind in winter (left) and summer (right) with the arrows indicating the upward gravity propagation (after *Lindzen*, 1981).

for summer and winter are given in Figure 2.2. In the summer hemisphere, a mean westward wind allows only gravity waves with an eastward phase speed to propagate up to the mesosphere, where they dissipate and deposit their momentum. The eastward momentum accelerates the air masses eastward, which by the Coriolis force results in a transport towards the equator. In the winter hemisphere, the drag induced by the westward propagating waves results in a poleward transport. This creates a global circulation, where air masses from the summer pole are transported all the way to the winter pole. To satisfy the continuity of mass, air from the lower atmosphere rises over the summer pole and descends over the winter pole. While rising, the upwelling air cools adiabatically, which leads to the low temperatures near the summer mesopause. In the winter hemisphere, the downwelling air creates the warm winter mesopause.

With typical wavelengths between 50 and 500 km, gravity waves are observable locally. Temperature and wind disturbances created by gravity waves can become visible in clouds as wave structures. These wave patterns do not only appear in tropospheric clouds but are also visible in the far higher noctilucent clouds. Wavelengths of a few kilometers, phase speed, and propagation direction of the waves in the mesopause region are derived from observations of noctilucent clouds with ground-based cameras and airglow imagers (*Witt*, 1962; *Pautet et al.*, 2011).

2.3 Noctilucent clouds

Noctilucent clouds (NLC) are the highest clouds in the Earth's atmosphere. With an average altitude of 83 km (e.g. *Jesse*, 1896; *von Zahn et al.*, 1998) they are much higher than the common clouds in the troposphere. Their observation was reported for the first time in 1885 (*Jesse*, 1885; *Leslie*, 1885; *Backhouse*, 1885). Noctilucent clouds are only visible after sunset when the sun is about 6° to 16° below the horizon. The NLC are still illuminated

Figure 2.3: Noctilucent clouds seen from Trondheim with small structures in the foreground.

by the sun because of their height and appear as silvery-blue seemingly glowing clouds (Figure 2.3). Even if the thin clouds are not visible during the day, they can exist at any time of day. An overview about noctilucent clouds is given in *Gadsden and Schröder* (1989).

Already *Wegener* (1912) suggested that NLC are composed of ice particles, but this was shown only in 2001 using solar occultation measurements and ice particle extinction spectra (*Hervig et al.*, 2001). In order for ice particles to form, the degree of saturation S given by the ratio of partial pressure of water vapor $p_{\mathrm{H_2O}}$ to the saturation pressure of water vapor p_{Sat}

$$S = \frac{p_{\mathrm{H_2O}}}{p_{\mathrm{Sat}}} \tag{2.10}$$

must by larger than 1. This condition is fulfilled only near the cold summer mesopause at high latitudes.

The ice particles form by heterogeneous nucleation near the temperature minimum of the atmosphere in the mesopause around 88 km. Aerosols, particles of the size of a few nm, possibly condensed meteor dust, serve as nuclei, on which the water vapor deposits if $S > 1$. Since the saturation ratios which are necessary for homogeneous nucleation are very high, this process is negligible (*Rapp and Thomas*, 2006). The small particles sediment downwards and continue to grow until they reach a region where $S < 1$. With the air no longer saturated, the ice particles sublimate.

The scattering intensity of the particles depends on their radius with a power of $\sim r^6$ according to Mie theory (*Witt*, 1968). The particles are small near the mesopause, such that the scattering is not yet strong enough to observe the clouds by eye or lidar. However, they can be observed by radar as polar mesospheric summer echoes (PMSE) starting at sizes of $\sim$5 nm (*Rapp and Lübken*, 2004). The particles are large enough to be detected as NLC when the radii reach 20–100 nm (e.g. *von Cossart et al.*, 1999), which is still much smaller than the ice particles in tropospheric cirrus clouds (*Baumgarten et al.*, 2002)

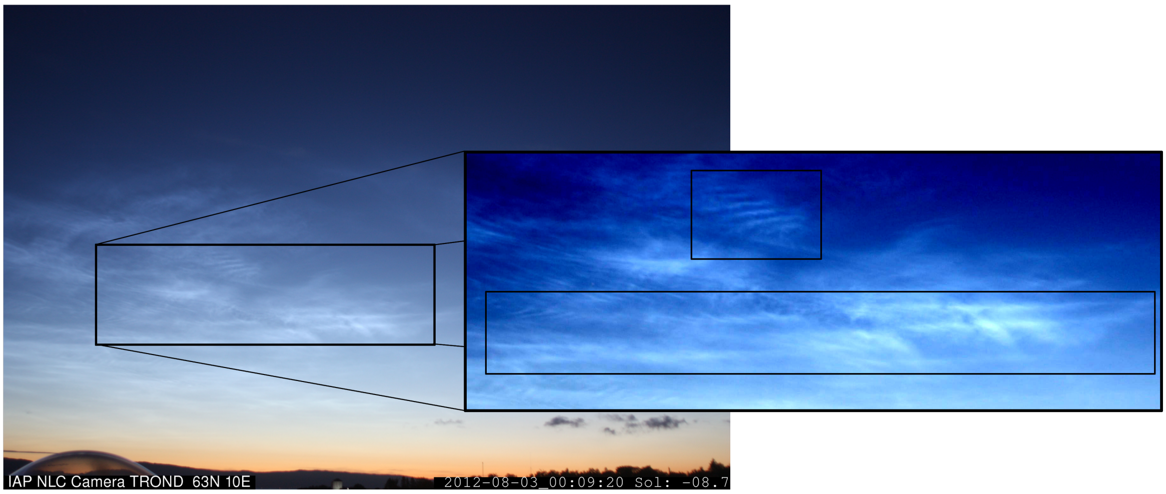

Figure 2.4: Different waves visible in an NLC picture taken at Trondheim, 00:09, 03 August 2012: Billows with a small wavelength are visible in the upper part and bands with a larger wavelength and larger horizontal extent in the lower part.

The mesosphere has for a long time been the least studied part of the atmosphere. Balloons that are used to study the troposphere and the stratosphere cannot reach altitudes higher than 40 km. Satellite orbits on the other hand only start at heights around a few hundred kilometers. In situ measurements in the mesosphere are possible only with sounding rockets, but they are not suited for continuous measurements. Temperature and wind profiles have been measured since 1960 up to the mesopause using rockets (*Stroud et al.*, 1960).
NLC respond sensitively to changes in the background atmosphere because of the very specific conditions necessary for them to form. Already a small increase in temperature can make the saturation ratio fall below 1 and the particles sublimate. The occurrence rates of NLC therefore depend on the temperature and its variations that reflect the dynamics of the middle atmosphere. The waves in the brightness of the NLC result from changes in the size or the number density of the ice particles and show the local variability of the temperature and the wind. However, whether NLC can also be used as an indicator for long term trends in the mesosphere has been subject to controversy (*Thomas*, 1996; *von Zahn*, 2003; *Thomas et al.*, 2003).

From the ground, the clearly visible and changing structures give an idea of the dynamic processes that govern the mesosphere. Depending on the wavelength, small scaled billows or ripples with wavelengths of 5–10 km and the larger bands with wavelengths around 50 km can be observed (*Witt*, 1962). Figure 2.4 shows a picture of an NLC, where wave structures are visible. The bands are manifestations of gravity waves, while the billows are short-lived instabilities created by the breaking of gravity waves (*Fritts et al.*, 1993). With automated cameras the NLC can be recorded and wave properties like horizontal wavelength, phase speed and propagation direction can be extracted from the images (*Pautet et al.*, 2011; *Demissie et al.*, 2014). Similar analyses are possible for satellite images (*Chandran et al.*, 2009).

The brightness of the NLC depends on the size of the particles and their number density. Gravity waves lead to perturbations in the wind and in the temperature that can reach more than 30 K in the mesosphere (*Höffner and Lübken*, 2007). However, on timescales of a few minutes, the growth of particles is a slow process compared to the short time scales of the smaller brightness variations. It is more probable that these are caused by wind variations that can affect the NLC by inducing a vertical undulation in the NLC layer or by changing the particle density by divergence and convergence (*Jensen and Thomas*, 1994). Gravity waves affect the growth of NLC particles by the induced changes in temperature on larger time scales. Models have shown that gravity waves with periods longer than 6.5 h tend to enhance NLC while shorter waves destroy them (*Rapp et al.*, 2002). However, a correlation of gravity waves and NLC occurrence or brightness could be confirmed only at some locations (e.g. *Chu et al.*, 2009; *Wilms et al.*, 2013).

NLC are a natural tracer for processes in the mesopause region that are difficult to study, while the observation of NLC is possible without any instrument. In the structured and changing brightness of the cloud as seen from the ground the dynamics of the atmosphere become visible by naked eye. The aerosol backscatter signal from the NLC ice particles is up to two orders of magnitude stronger than the Rayleigh scattering of the air, which makes them detectable by lidar. With the appropriate filtering they can be detected even during the broad daylight that makes up most of the NLC season at higher latitudes.

The first measurements of NLC by lidar were realized by *Hansen et al.* (1989) in northern Norway. Continuous measurements of NLC every summer provide the means of long time studies over several years (*Fiedler et al.*, 2005). Lidar measurements are only possible during clear sky conditions. Then they offer the advantage of continuous high resolution measurements over days, if permitted by the weather. The possibility to measure continuously during day and night makes the lidar more reliable for occurrence rate and trend studies than the camera observations from the ground. The lidar also provides the brightness of the clouds in height and time at a resolution high enough to observe the same structures that are seen from the ground.

Besides the ground based observations, satellites and sounding rockets contribute to NLC measurements. NLC were first measured from space with the OGO-6 satellite (*Donahue et al.*, 1972). From different satellites NLC have been detected with instruments that were originally not designed for NLC measurements, including trend studies over 20 years from SBUV instruments for ozone measuring (e.g. *DeLand et al.*, 2003). In 2007, the AIM (Aeronomy of Ice in the Mesosphere) satellite was launched, the first satellite with instruments specifically for observations of NLC, or polar mesospheric clouds (PMC), as NLC are called when observed from space (*Rusch et al.*, 2009). The NLC brightness measured by the CIPS (Cloud Imaging and Particle Size) instrument on AIM corresponds to the vertically integrated NLC backscatter coefficient measured by lidar, allowing a comparison of the observations (*Baumgarten et al.*, 2012). Satellites provide measurements on global scales, independent of the weather conditions. Depending on the orbit, they cover up to the whole summer hemisphere. Unlike the lidar, they do however not provide the data for high resolution time series.

3 Instruments

The NLC lidar data is obtained at the ALOMAR (Arctic Lidar Observatory for Middle Atmosphere Research) observatory on the island of Andøya, Norway, at 69° N (Figure 3.1). The NLC are measured with the Rayleigh/Mie/Raman (RMR) lidar at the observatory. Since 1994, measurements of NLC have been conducted every summer, providing a large dataset for long time studies of NLC (*Fiedler et al.*, 2011). Besides the RMR lidar, the instruments at ALOMAR include a sodium lidar and several radars, which operate in the same area and provide complementary data like the background wind or PMSE observations. At the nearby Andøya Space Center, sounding rockets are launched to perform in situ measurements in the same measurement volume. The region is furthermore covered by the CIPS measurements from the AIM satellite, providing horizontally resolved images of NLC that are independent of the weather conditions (*Russell et al.*, 2009; *Lumpe et al.*, 2013) The combination of the different instruments at the same location has been used to compare and relate the different observations (e.g. *Nussbaumer et al.*, 1996; *Baumgarten et al.*, 2009; *Kaifler et al.*, 2011).

3.1 Rayleigh/Mie/Raman lidar

The lidar (light detection and ranging) is an instrument for remote sensing based on a similar idea as the radar. A laser pulse is sent out into the atmosphere, where it is scattered by molecules and particles. A telescope detects the backscattered light as a function of time. The time between the emission of the pulse and the detection of the signal is converted to the altitude where the scattering process took place.

Different processes contribute to the backscattered signal. Always present is the Rayleigh scattering from the air molecules of the atmosphere. The signal is proportional to the air

Figure 3.1: ALOMAR observatory in northern Norway. The two tilted laser beams from the Rayleigh/Mie/Raman lidar are visible.

density and therefore decreases exponentially with altitude. The larger aerosols or cloud particles scatter the light according to the Mie theory. When clouds are present, this signal is much stronger than the Rayleigh scattering.

At 69° N, the sun does not set for two months from mid-May to mid-July. To measure during the NLC season despite the permanent sunlight, the lidar must be daylight capable. The daylight observations require that the part of sunlight among the detected photons is reduced to a minimum. To this end, telescopes with a small field of view are needed to lower the part of incoming solar photons. Therefore, the divergence of laser beams must be small, and the beams must be stabilized into the field of view of the telescopes. The backscattered light is filtered spectrally by a Fabry-Perot etalon that removes most of the solar background while still being large enough to include the Doppler broadened Rayleigh signal.

The RMR lidar at ALOMAR consists of a twin lidar system with two lasers that emit light at three different wavelengths: 355 nm, 532 nm and 1064 nm. The two Nd:YAG lasers with 30 Hz pulse repetition rate are seeded by a single cw laser stabilized on an iodine absorption line. The position of the laser beam is stabilized, before the beam diameter is increased to 20 cm using a beam widening telescope. This ensures a small divergence of the laser beam of $\leq 70\,\mu\text{rad}$, which allows for the backscatter volume to be inside the field of view of the telescopes. The position of the laser beam is actively stabilized by mirrors that adjust their position based on the recorded image of the laser beam with a CCD camera inside the telescope. The backscattered light is detected by two quasi-Cassegrain telescopes with primary mirrors of 1.8 m diameter. The telescopes can be tilted up to 30° from zenith, one in the north-west (NWT) and the other in the south-east (SET) quadrant. The laser beams are aligned with the axis of the telescope by beam guiding mirrors and are tilted with the telescopes. Figure 3.2 shows an image of both telescopes in a tilted position during a measurement. The combination of both lidar systems in a tilted configuration allows to measure the same NLC at different positions. A detailed description of the RMR lidar is given in *von Zahn et al.* (2000).

The lidar equation describes the detected intensity I at the emitted wavelength λ and the altitude z, which is given by the time between the emission and the detection of the signal t and the speed of light c as $z = 1/2 \cdot ct$.

$$I(\lambda, z) = I_0(\lambda)\left(\frac{A}{z^2}\right)\beta(\lambda, z)T^2(\lambda, z)\eta(\lambda)\Delta z, \tag{3.1}$$

with the emitted intensity I_0, the area of the telescope A, and the detector efficiency $\eta(\lambda)$. The transmission T through the atmosphere is given by $T = \exp\left(-\int_0^z \alpha(z', \lambda)\mathrm{d}z'\right)$ according to the Beer-Lambert Law with the extinction coefficient in the atmosphere $\alpha(z, \lambda)$ (e.g. *Wandinger*, 2005).

The total backscatter coefficient $\beta(z)$ consists of the backscatter coefficient from the air molecules $\beta_\mathrm{m}(z)$ and from the NLC $\beta_\mathrm{NLC}(z)$. To obtain the NLC backscatter coefficient β_NLC or brightness of the NLC, the signal of the Rayleigh background of the atmosphere has to be removed. From the raw photon count the signal $S(z)$ is derived by subtracting the solar background and the thermionic emission of the detectors. The backscatter ratio $R(z)$ is defined as the ratio of $S(z)$ to the backscatter signal from air molecules $S_\mathrm{m}(z)$ or

Figure 3.2: Telescopes at the ALOMAR observatory in a tilted position with the protective covers over the primary mirrors opened. The beam guiding mirrors positioned over the telescopes align the laser beams coaxial to the telescopes and stabilize the beam into the field of view of the telescopes.

equivalently the ratio of the volume backscatter coefficients $\beta(z)$ and $\beta_\mathrm{m}(z)$.

$$R(z) = \frac{S(z)}{S_\mathrm{m}(z)} = \frac{\beta(z)}{\beta_\mathrm{m}(z)} = \frac{\beta_\mathrm{m}(z) + \beta_\mathrm{NLC}(z)}{\beta_\mathrm{m}(z)} \tag{3.2}$$

The volume backscatter coefficient from NLC is defined as

$$\beta_\mathrm{NLC}(z) = n_\mathrm{NLC} \cdot \left.\frac{\mathrm{d}\sigma(180°)}{\mathrm{d}\Omega}\right|_\mathrm{NLC,} \tag{3.3}$$

with n_NLC the number density of NLC particles and $\left.\frac{\mathrm{d}\sigma(180°)}{\mathrm{d}\Omega}\right|_\mathrm{NLC}$ the backscatter cross section that depends on the particle size and shape. From the measured signal, $\beta_\mathrm{NLC}(z)$ is computed with

$$\beta_\mathrm{NLC}(z) = (R(z) - 1) \cdot \beta_\mathrm{m}(z). \tag{3.4}$$

The molecular backscattering $\beta_\mathrm{m}(z)$ is derived from the density. For the density values, the absolute densities from *Lübken* (1999) above 55 km are combined with the normalized relative densities measured by the lidar below 55 km. $S_\mathrm{m}(z)$, proportional to $\beta_\mathrm{m}(z)$, is then normalized to $S(z)$ at 35 km (*Baumgarten et al.*, 2002).

The uncertainty on the signal and on the subtracted background contribute to the uncertainty on the brightness β_NLC. For both quantities a Poisson distribution is assumed and the error is calculated using error propagation. Variations in the density on small time scales that are not taken into account in the normalization add another small uncertainty (*Müller*, 2009).

The data are integrated over 1000 pulses. With a laser frequency of 30 Hz this corresponds to a time resolution of 33 s. The data is then interpolated on a grid with a resolution of 30 s and 40 m, available since 2008. For comparison with data from previous years or from other lidars, lower resolution data are also available. Additionally, the lidar single shot acquisition (LISA) records the backscatter signal for each single laser shot, which corresponds to a temporal resolution of 33 ms.

During the NLC season from June to August the lidar is operated on campaign basis. Measurements are done whenever it is allowed by the weather. The regular upgrade of components of the detection system has improved the sensitivity and the resolution of the system over the years (*Fiedler and Baumgarten*, 2012).

3.2 Saura MF radar

For the wind measurements in the mesosphere radar data are used. The Saura mid frequency (MF) radar is located near the ALOMAR observatory and covers a height range from 40–103 km with a height resolution of 1 km and 30 min time resolution (*Singer et al.*, 2008). Electromagnetic pulses are transmitted into the atmosphere where they are scattered and reflected at irregularities of the refractive index. In the mesosphere, the irregularities in the refractive index arise from variations in the electron density.

To measure the wind field, the motion of the scattering structures and thereby the wind is deduced from the scattered wave detected by the antenna field. The Doppler Beam Swinging (DBS) method uses the Doppler shift of the detected signal that yields the wind speed. From the measurement in one direction, the wind in the line of sight can be derived. Combined measurements in different directions give the horizontal wind vector.

4 Data analysis

4.1 Motivation

The NLC data is available as volume backscatter coefficient $\beta(z,t)$ per time t and altitude z at a resolution of 30 s and 40 m at ALOMAR since 2008. Part of the data have previously been analyzed with focus on small scales using characteristic time series extracted from the two-dimensional data (e.g. *Kaifler et al.*, 2013). Variations in the altitude can be described by the top and bottom altitude, the altitude of maximum brightness z_{Peak}, or the centroid altitude z_{C}, defined as the weighted mean of the height with the cloud brightness for each bin i.

$$z_{\text{C}} = \frac{1}{\sum_i \beta(z_i)} \left(\sum_i z_i \beta(z_i) \right) \tag{4.1}$$

With this definition of z_{C}, the time series does not contain sudden jumps as would be possible with z_{Peak}, if the brightest layer is not clearly defined. The difference between z_{Peak} and z_{C} is shown in Figure 4.1. Similarly, the maximum, mean, and column integrated backscatter coefficients yield time series for the cloud brightness. From these time series, the spec-

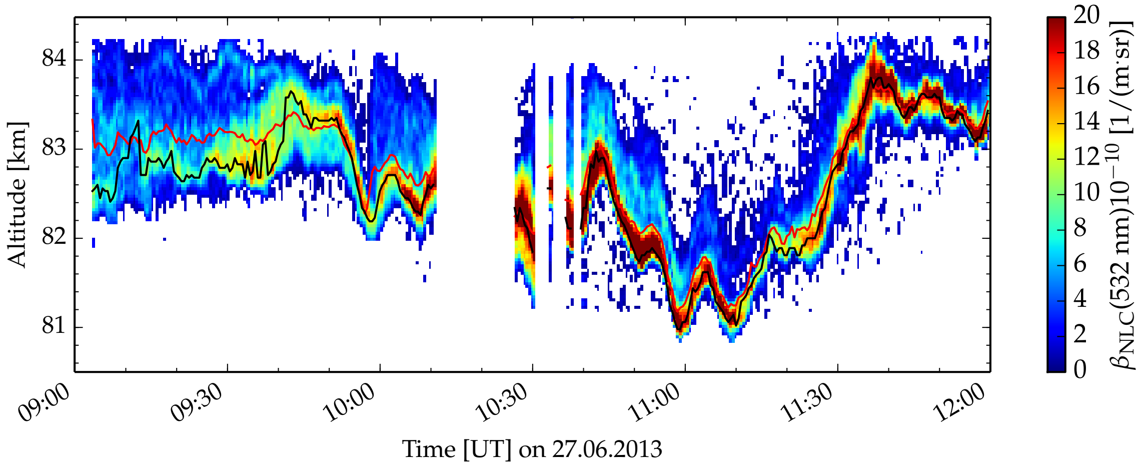

Figure 4.1: High resolution lidar data of an NLC. Shown in red is the centroid altitude z_{C} and in black the altitude of maximum brightness z_{Peak}. The difference between z_{C} and z_{Peak} becomes obvious around 09:15, where z_{Peak} varies between different layers of higher brightness while z_{C} is smooth. Waves in the NLC layer with periods in the order of minutes and hours are visible in the two dimensional β_{NLC} data as well as in the centroid altitude. Gaps in the data like at 10:10–10:25 indicate interruptions of the measurement often caused by passing clouds.

trum of the respective quantity can be computed with a Fourier or wavelet transform.

However, a Fourier or a wavelet analysis has several shortcomings. As the lidar measurements are possible only during clear sky conditions or with very thin clouds, passing clouds or longer deterioration of the weather result in frequent gaps of variable length in the data. Clouds may be forming often and quickly because of the location of the observatory on a small mountain near the coast in a marine climate. For a wavelet analysis, irregularities in the time series have to be dealt with. The analysis can be limited to continuous parts of the data or the data could be interpolated beforehand. An alternative is the Lomb-Scargle periodogram, conceived as a way to analyze time series with unevenly spaced data (*Lomb*, 1976; *Scargle*, 1982). Details about the Lomb-Scargle analysis are given in Section 4.5.

The wavelike variations in the altitude of the NLC layer are clearly visible in the $\beta_{\mathrm{NLC}}(z,t)$ data without further processing as shown in Figure 4.1. However, there exist cases where there seem to be no waves on small scales or the waves are limited to certain parts of the NLC. Figure 4.2 shows an example of an NLC where no small wave structures are apparent during the first part of the measurement. A distinction between those parts and apparent waves is not possible considering only the centroid altitude. Therefore it is not possible to systematically extract the properties while ignoring the unstructured parts by using only a wavelet transform. Furthermore all information about the vertical structure of the NLC is lost by using the centroid altitude. Multiple layers, occurring occasionally in NLC, should be identified and separated before the analysis.

A different approach is used here, in order to avoid these problems. In the two dimensional NLC data, the visible wave structures in the NLC layer are identified by an image based pattern recognition algorithm. Some information about the waves is directly available from the identified patterns, like a measure of the wave activity based on the number of detected waves, the length of the wave patterns or the presence of multiple layers. The NLC

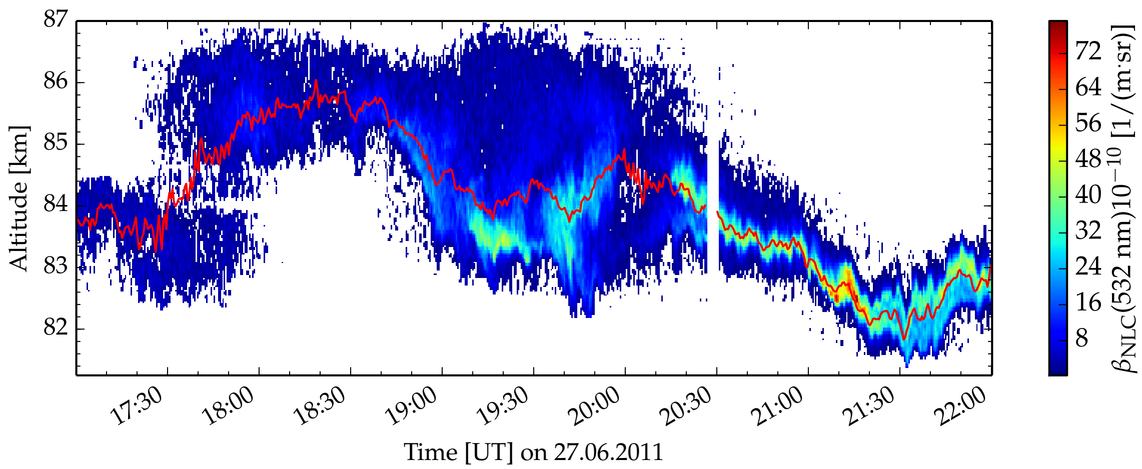

Figure 4.2: High resolution observation of an NLC, where no small scale structures are visible before 19:30. Between 21:00 and 22:00, pronounced wave structures are visible. A distinction between such regions in time and altitude with wave structures from less structured regions is not possible using only the centroid altitude z_c (red). Additionally, the multiple layer at 17:30–18:00 cannot be seen in z_c.

is effectively reduced to the parts during waves, where small scale variations are present. The Lomb-Scargle periodogram of the centroid altitude which takes into account only the parts with detected variations provides a reliable way to determine the periods of these variations even on small scales. The algorithm is explained in the following using the data from the 27. June 2013 as an example.

4.2 Preprocessing

The data used in this work has already been preprocessed as follows: From the raw NLC brightness profiles obtained after subtraction of the background as described in Section 3.1, values for β below a threshold are removed, as to keep only the NLC data and no background fluctuations. An NLC probability based on the adjacent pixels helps to remove single high values in the background that pass the threshold. This analysis is applied to low resolution data to determine the shape of the NLC, which is then applied as a mask to the data of higher resolution. The data obtained this way contain only the profiles of the NLC and the values in its immediate vicinity (*Müller*, 2009).

For the detection of small scale variations, further processing has been applied. The data contain frequent gaps, ranging from minutes to hours, that are in most cases due to the changing weather conditions. Small passing clouds can reduce the signal temporarily, such that no significant signal is detected. During cloudy conditions, the measurement is stopped completely, resulting in longer interruption of the data. Finally, changes in the system, like tilting of the telescopes, causes small gaps in the data. If only a few values are missing but the wave structure is still recognizable, the missing values can safely be ignored for the pattern recognition. The analysis targets small scales up to 2–3 hours in the NLC data, therefore gaps up to 1 h are left in the data as they are. When the separation between the NLC measurements becomes larger than 1 h, the NLC is split into separate segments. To reduce the noise, an NLC must consist of at least 5 adjacent data points in either height or time to be taken into account.

For the pattern recognition, the remaining data is smoothed, using a two dimensional Gaussian filter. The width of the Gaussian determines the scale of the structures that can be found. A filter with a width similar to the data resolution enhances the similarity with the templates by removing small irregularities. If the data is smoothed with a broader filter, the resolution of the data is reduced. Without the small structures, the same pattern recognition can then be used to find larger wave structures. Figure 4.3 shows the original data and Figures 4.4 and 4.5 the data after after applying Gaussian filters of different widths.

4.3 Pattern recognition

In the next step, the preprocessed data is searched for wavelike patterns. The characteristic wave patterns of the NLC layer are visible in almost every measurement. However, some clouds are considerably more structured than others. The extraction of these wave features can be used to quantify the amount of waves, as well as their characteristics. The method used here is based on the *matchTemplate* function from the open source computer vision library *openCV* for *Python*.

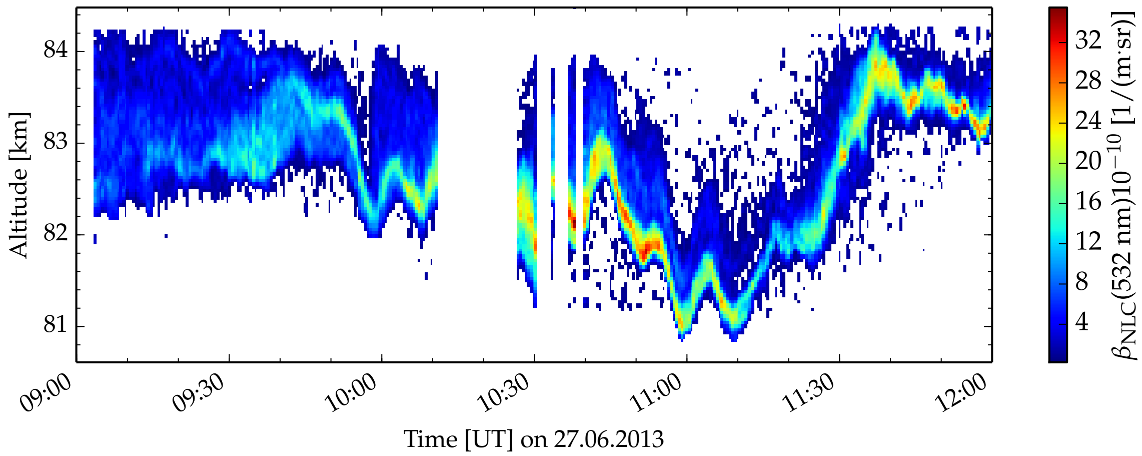

Figure 4.3: Original data of the NLC on the 27. June 2013. The background where $\beta_{\text{NLC}} = 0$ is masked.

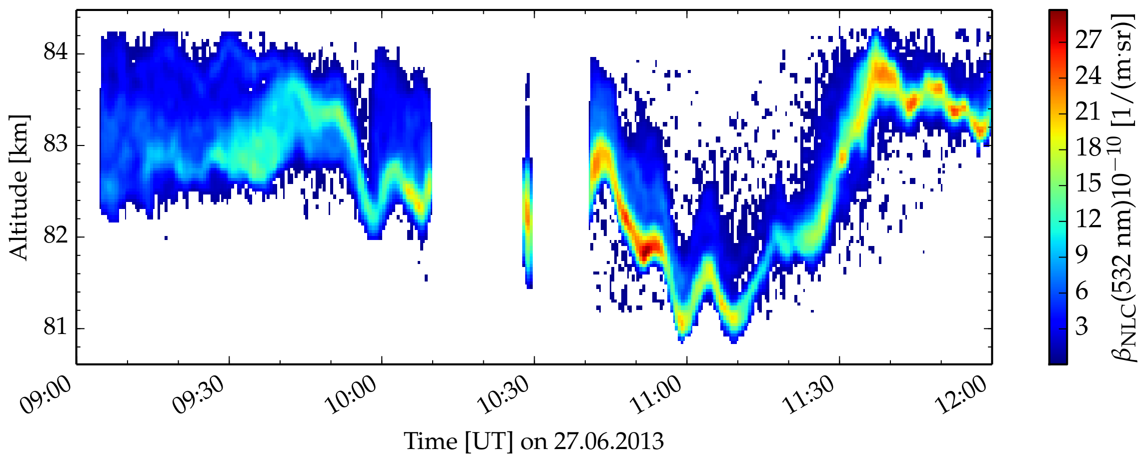

Figure 4.4: NLC on the 27. June 2013, smoothed with a Gaussian of width $\sigma = 1$ bin (corresponding to 30 seconds · 40 meter) used to detected periods < 1 h.

A query image I of size $M \times N$ is searched for a smaller template image T of size $m \times n$ by means of the cross-correlation. The template is shifted over the query image and at each position, the cross-correlation coefficients are computed. The result is an output array R of size $(M - m) \times (N - n)$ with values ranging from -1 to 1:

$$R(x,y) = \frac{\sum_{x',y'} \left(T'(x',y')I'(x+x',y+y')\right)}{\sqrt{\sum_{x',y'} \left(T'(x',y')^2 I'(x+x',y+y')^2\right)}} \tag{4.2}$$

with the template

$$T'(x',y') = T(x',y') - \frac{1}{m \cdot n} \sum_{x''.y''} T(x'',y'') \tag{4.3}$$

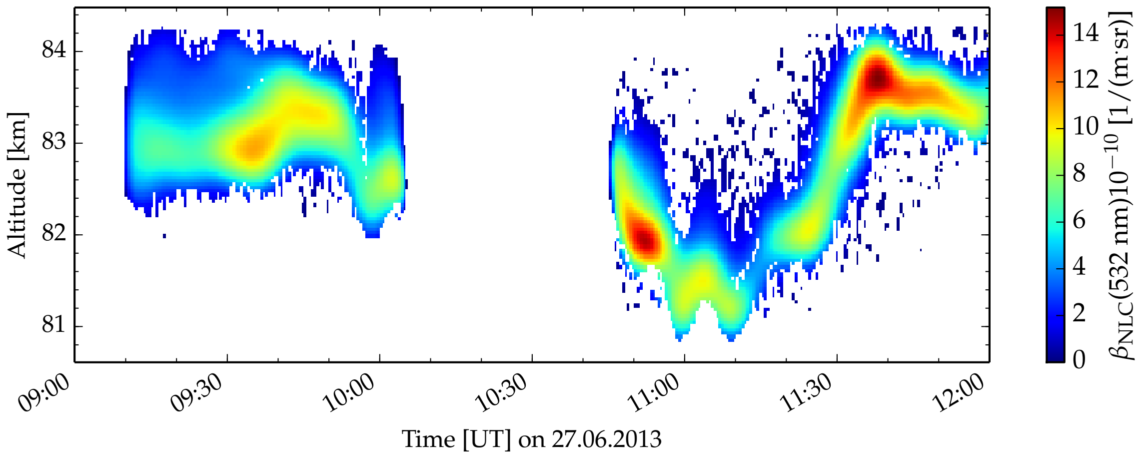

Figure 4.5: NLC on the 27. June 2013, smoothed with a Gaussian of width $\sigma = 5$ bins (150 seconds · 200 meter), used to detect periods > 1 h.

and the part of the query image at (x, y) of the size of the template

$$I'(x + x', y + y') = I(x + x', x + y') - \frac{1}{m \cdot n} \sum_{x'', y''} I(x'', y''). \tag{4.4}$$

A perfect match between the template and the query image corresponds to a value of 1. The computation is extended by repeating the search for the same template scaled over a range of different sizes in both dimensions.

The wave patterns in the NLC are diversified on longer time scales, but can be broken down into sequences of single "V" and "Λ" shaped oscillations. The preprocessed data is searched for templates representing these single oscillations. As minimum size of the template a duration of 5 min is chosen for smallest scales. With a time resolution of 30 s, this corresponds a length of 10 points. The same minimum of 10 points is imposed for the height of the template, corresponding to 400 m, such that the template consists of at least 100 pixels. For smaller templates, variations cannot be distinguished reliably from noise. The maximum size is fixed to 30 min, since in most cases, longer oscillations are superposed with waves with higher frequencies, such that they will not be recognized by the algorithm. To identify these waves, the data smoothed with a Gaussian of larger width is used and the template size range is increased to 25–100 min.

From the cross-correlation coefficients, the positions of successful matches are extracted as the maxima of connected areas above a threshold. The results of the *matchTemplate* routine for a single template are shown in Figure 4.6 with the positions where the cross-correlation coefficient is higher than the threshold, which corresponds to a detected structure. All results with an error to brightness ratio larger than 0.3 are not taken into account, as in these cases the difference between noise and wave structure becomes unclear. The same algorithm is again applied to the data, with the templates detecting "V" shaped structures turned about 180° which results in the corresponding inverse "Λ" shaped wave structures.

The parameters and the different patterns are determined by visual inspection and test-

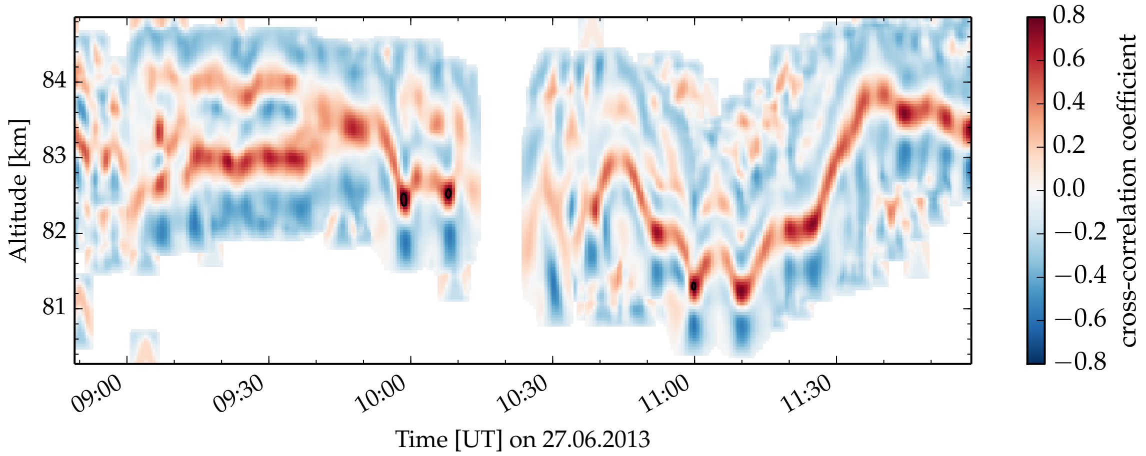

Figure 4.6: Cross-correlation coefficient R for template 3 (see Figure 4.7 for the definition of the templates) with width $m = 11$ and height $n = 24$. The areas where the templates matches the NLC structure i.e. the cross-correlation coefficient is higher than the threshold value ($R > 0.8$) are marked in black.

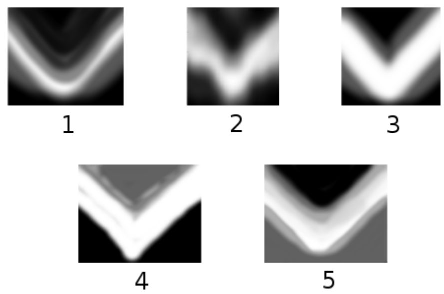

Figure 4.7: Templates used for the pattern recognition with intensity values from 0 to 255. The NLC data are converted to gray scale before running the pattern recognition, with 0 for no NLC (masked in plots) and 255 for maximum brightness. Templates 1 to 3 differ by the width of the bright layer on a dim background. The templates 4 and 5 target structures at the top and bottom of the NLC.

ing on the data of the year 2013 with 339 h of NLC measurements. Based on these results, the threshold value is set to 0.8, which includes what one would identify visually as characteristic variations. The majority of the wave structures in the NLC is successfully detected with 5 slightly different templates. In Figure 4.7, the five templates that were used for the pattern recognition are shown. The width of NLC layers can vary from a few hundred meters up to kilometers, which cannot be accounted for with a single template. Examples for characteristic results for the different templates are shown in Figures 4.8–4.10. Template 1 (Figure 4.8) occurs in only very few cases, where the layer width is small compared to the size of the variation and has a sinusoidal shape. While the occurrence of template 1 is very low, it is necessary to detect the larger structures with small layer width that will not be found by the other templates. Template 2 and 3 are very similar and account for most of

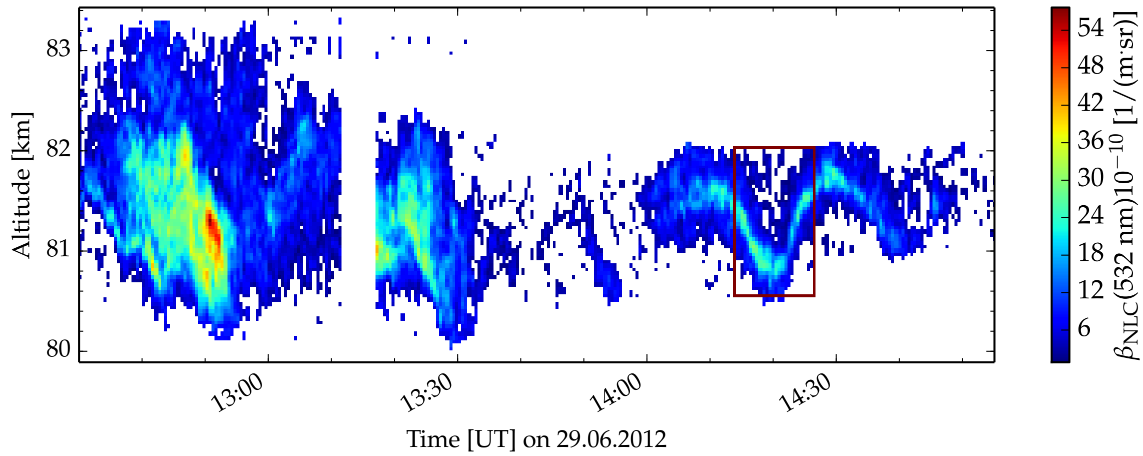

Figure 4.8: Example for template 1

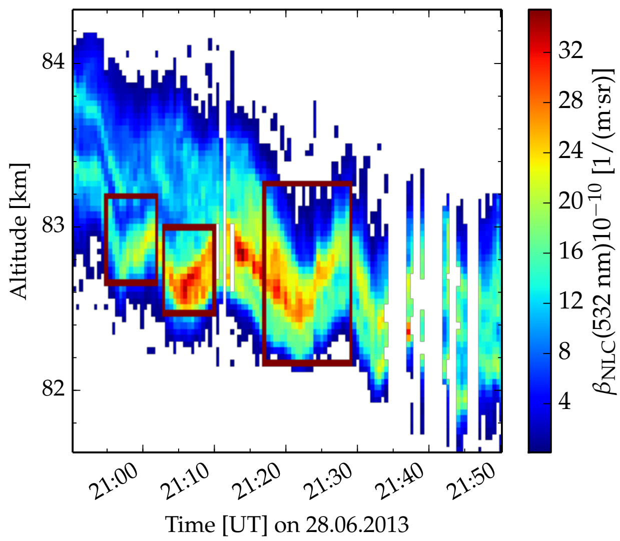

Figure 4.9: Example for templates 2 and 3. The leftmost variation has the highest correlation with template 2. The thicker layers in the middle and right structures correspond best to template 3.

the results. Template 2 is taken as typical variation from real NLC data, while template 3 is synthetic. The difference is here again the layer width, that is higher for template 3 (Figure 4.9). The high occurrence of both templates shows that a template based on NLC data is as suited for the pattern recognition as a synthetic template. Finally, template 4 and 5 cover a more specific type of structures that appear in NLC. As shown in Figure 4.10, template 4 targets variations where the difference in brightness is only distinct above the variations, while below the brightness decreases only slightly. This kind of pattern is often seen at the top of the NLC, where the variation does not manifest by the altitude modulation of a thin layer of higher brightness but only by the variation of the top altitude of the NLC.

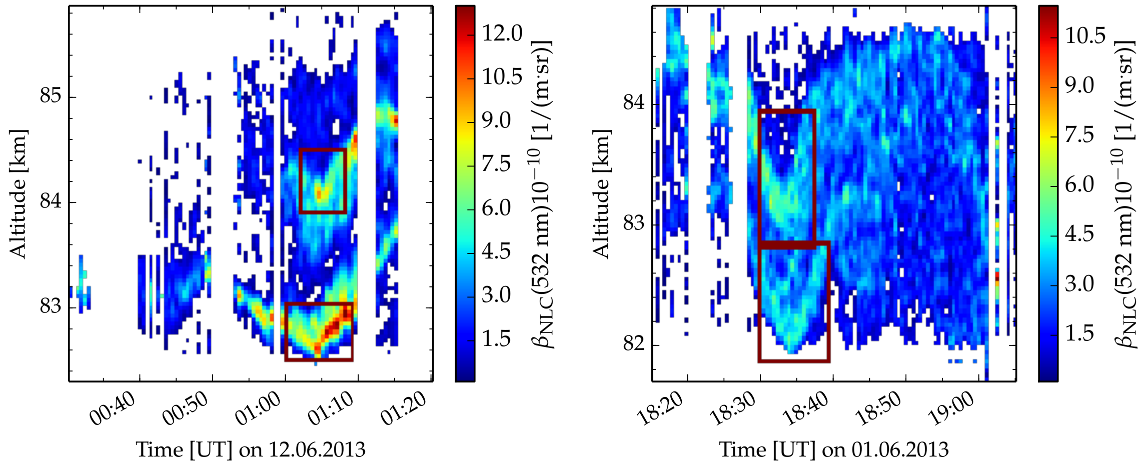

Figure 4.10: Examples for templates 4 (lower match) and 5 (upper match). In the right plot, the brightness does not decrease sufficiently between the two layers for the other templates to pass the threshold.

Template 5 is the complementary template for the lower end of the NLC. Moreover, both templates are important for double layers with a small vertical distance, where the brightness of the layer does not decrease strong enough for the structure to be found by the other templates.

The pattern recognition algorithm is similar to a wavelet analysis. However, it is not limited to a specific wavelet but can be used with arbitrary structures. The template with a single exemplary oscillation corresponds to a narrow wavelet. Instead of a time series, the two dimensional NLC data are used directly. The template is shifted over the data and scaled to cover various periods, as is the wavelet in the wavelet transform. The resemblance between template and the data is defined by the convolution instead of the cross-correlation for the wavelet analysis. The convolution $(f * g)(t)$ is equivalent to the cross-correlation of $f(t)$ and $g(-t)$. However, for the method used here, no evenly spaced data is necessary. All the examples in Figures 4.8–4.10 cannot be directly analyzed by a wavelet transform because of the gaps in the time series caused by tropospheric clouds.

The objective of the pattern recognition is not to obtain a power spectrum as for a wavelet analysis, therefore only the significant results with a high correlation are kept for further analysis. From the many results for the same structure with slightly different sizes and from different templates only the result with the highest cross-correlation coefficient is used. The final results for all templates are shown in Figure 4.11.

4.4 Wave patterns

In most cases, the waves in the NLC consist of more than one period, forming a wave pattern that can extend over hours. The detection of the single oscillations only yields the elementary wave structure. The single wave structures overlap and can be combined to longer, more complex wave patterns. To identify those more varied structures, the single wave elements extracted with the pattern recognition are checked for adjacent variations

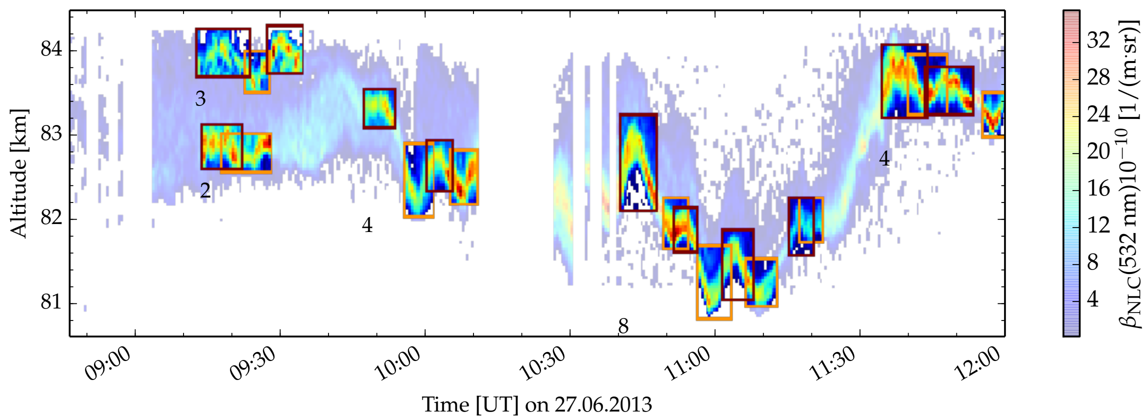

Figure 4.11: Detected wave structures from all 5 templates in both "V" (orange) and "Λ" (red) orientation. Continuous wave patterns appear as sequences of alternating "V" and "Λ". The numbers denote the number of detections forming the pattern.

that might be part of the same wave pattern. Based on the position and the size of the results, an algorithm joins them to wave patterns with several periods, while keeping separated those that belong to different layers or that are disconnected. In Figure 4.11, the number of single oscillations that form the wave pattern is noted beside the corresponding pattern.

4.5 Lomb-Scargle periodogram

The wave patterns found by the pattern recognition algorithm are those parts of the NLC where the brightness layer is visibly modulated by a wave. To extract the frequency of this wave, different approaches are possible: An estimation for the period is given by the size of the template for each single result. However, this length can correspond to a whole period or more as well as only half a period or even less, depending on the shape of the wave with the best correlation with the template. Another method would be to use the wave patterns identified previously instead of each single oscillation. Every detected wave element inside the wave pattern then accounts for half a period and the ambiguity only applies to the outermost results for each wave pattern.

Instead of relying on the results based only of the length of the detection to determine the period, they can be used only as a way to identify the regions where waves are visible and as a rough estimate of their period. For a more precise estimate of the period, the centroid altitude z_C is computed for each wave pattern, taking into account only the data from the pattern recognition as shown in Figure 4.12. For this time series, the power spectrum is computed using the Lomb-Scargle method (*Lomb*, 1976; *Scargle*, 1982). The Lomb-Scargle method is suitable for the spectral analysis of unevenly sampled data, including the case of missing data. The normalized Lomb-Scargle periodogram (spectral power as a function of the angular frequency $\omega = 2\pi f$) for a time series X_j with mean $\overline{X} = 0$ and variance $\sigma^2 = 1$

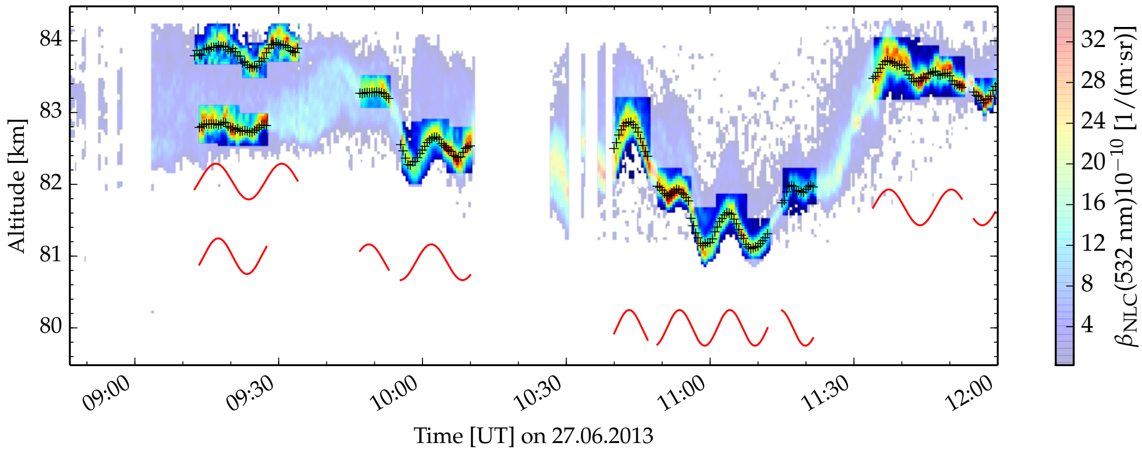

Figure 4.12: Identified wave patterns with the centroid altitude (black) and a monochromatic sine wave with the frequency from the Lomb-Scargle analysis (red) for verification.

is defined by

$$P_X(\omega) = \frac{1}{2}\left(\frac{\left(\sum_j X_j \cos\omega(t_j-\tau)\right)^2}{\sum_j \cos^2\omega(t_j-\tau)} + \frac{\left(\sum_j X_j \sin\omega(t_j-\tau)\right)^2}{\sum_j \sin^2\omega(t_j-\tau)}\right) \tag{4.5}$$

with τ

$$\tan(2\omega\tau) = \frac{\sum_j \sin 2\omega t_j}{\sum_j \cos 2\omega t_j}. \tag{4.6}$$

This definition of the periodogram corresponds to a least-square fit of sine waves with frequencies ω to the data. The periodogram is evaluated for a frequency range from the lowest frequency $f_{\text{min}} = {}^1/T_{\text{max}}$ with T_{max} the duration of the input data to a multiple of the Nyquist frequency f_c:

$$f_{\text{max}} = h \cdot f_c = h\frac{1}{2\Delta T} \tag{4.7}$$

with ΔT the sampling rate and the oversampling factor $h = 1.5$ (*Press*, 1992).

In the neighborhood of the estimated period based on the length of the detected variations, the spectrum is searched for significant maxima, which represent the mean period of the wave. The Lomb-Scargle periodogram for two exemplary wave patterns with the limits imposed by the period estimate and the final result for the period is shown in Figure 4.13. The frequency found this way corresponds well to the mean frequency of the observed waves, as can be seen in Figure 4.12, where a monochromatic sine wave with the determined period is overlaid to each wave pattern in the NLC data for a visual comparison. Periods smaller than 5 minutes can be determined by the Lomb-Scargle periodogram, even if the length of the template is limited to at least 10 points. This can happen if the variation is smaller than the template size, but the correlation is still high enough to pass the threshold.

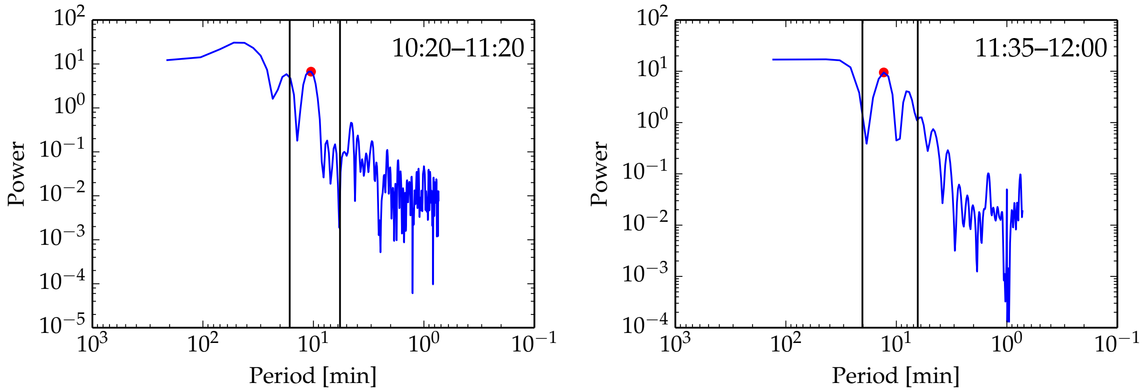

Figure 4.13: Normalized Lomb-Scargle periodogram for two exemplary waves on 27. June 2013. The black lines indicate the range delimited by the frequency estimate based on the length of the waves of the pattern recognition. The maximum inside this range (red) is taken as period for the wave.

4.6 Estimation of the horizontal wavelength

The variations of the NLC layer height observed in the lidar data are the result of local changes in the NLC and of the wind, that displaces the NLC through the laser beam. While the data from lidar observations do not permit to separate these two effects, it is assumed that NLC do not change significantly on small scales. The variations in time observed by the lidar then correspond to spatial variations in the NLC and can be used to determine the horizontal wavelength. For most NLC data, the wind at the same height is available from the Saura MF radar with a resolution of 1 km in altitude and a temporal resolution of 30 min as shown in Figure 4.14.

With the mean wind u_0 at the altitude and over the temporal extent of the detected wave structure, an estimate for the horizontal wavelength λ_h can be derived using the computed period T with $\lambda_h = u_0 T$, as shown in the schematic representation in Figure 4.15. The so calculated scale corresponds to the wavelength in the direction of the flow, assuming that the wave is parallel and the wave fronts are orthogonal to the background wind. This corresponds to the horizontal scale of the structure. With the wind from a different direction, the measured wavelength is longer than the actual horizontal wavelength of the wave.

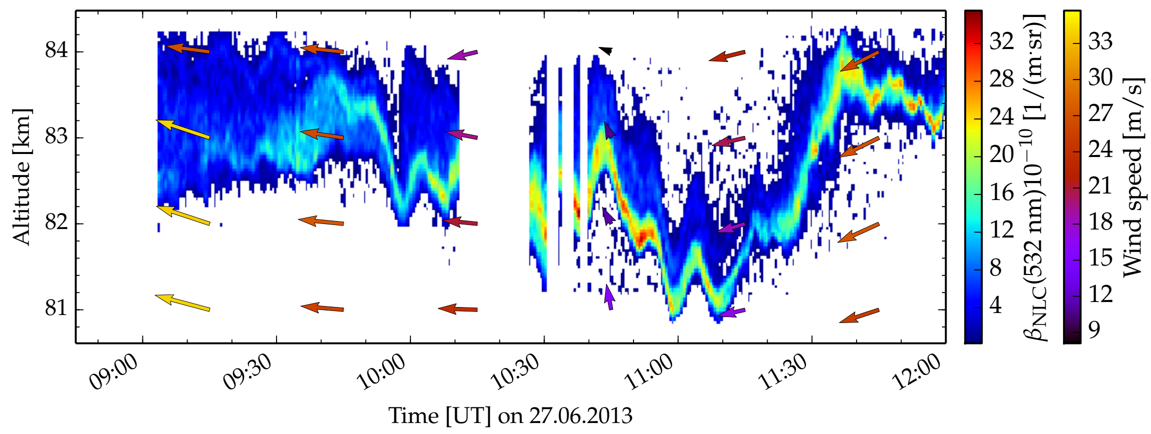

Figure 4.14: Background wind measured by the Saura MF radar during the NLC measurement. The arrows indicate the horizontal wind direction and speed at a certain altitude and time. Arrows pointing to the left or up indicate a westward or northward wind, respectively.

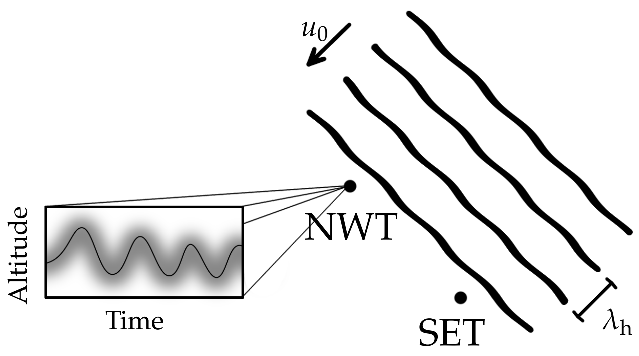

Figure 4.15: Relationship of the period measured with the lidar to the horizontal wavelength of the wave. The wave structure in the NLC with the wavelength λ_h is detected by the lidar as a variation in time with the period T, due to the advection by the background wind u_0.

5 Results

The analysis presented in the previous chapter is applied to the data set of five years from 2009 to 2013. The NLC lidar data are available in a 30 s time resolution and 40 m altitude resolution since 2008. For the computation of the wavelength, simultaneous wind data in the mesopause region are necessary. However, the wind measurements from the Saura radar were available only since 2009.

The NLC season extends from 1 June until 15 August. From 2009 to 2013 the data set consists of 2905 h of lidar measurements in the NLC season, 1219 h with the North-West Telescope (NWT) and 1686 h with the South-East Telescope (SET) system. During 947 h of these measurements NLC were detected. The difference of more than 400 h in the measurement time between the two systems was caused by the laser of the north-west system, that was not operational during the NLC campaign of 2011.

In 2013, the first NLC was measured on 21 May, one week earlier than in the last 15 years. This early appearance is caused by an unusual early cooling of the mesopause region (*Fiedler et al.*, 2014). Besides this early appearance in 2013, only a few NLC are detected out of season, the latest one on 20 August 2012. In total, 43 additional hours of NLC have been measured from 20 May to 20 August, which are included in the analyzed data set.

The usual measurement setup consists of one hour of observation with both lasers in zenith. After one hour, the telescopes are tilted by 20° from zenith, with the north-west system oriented northward and the south-east system oriented eastward. In this configuration, the NLC volumes targeted are separated by about 40 km. The measurements of the same NLC by tilted lasers are similar on time scales of several hours, thus much larger than the scales considered in the extracted wave patterns. On small scales, the waves detected in the NLC can differ significantly, due to the larger spatial distance. In the following statistics, the simultaneous measurements by both systems are considered as independent measurements, given the small part of zenith measurements.

The analysis is applied at two different scales. For small scales, corresponding to periods of up to 1 h, the data is smoothed with a Gaussian filter with a width of 1 data point (30 s×40 m). The template size is varied from 5 to 30 min. For larger scales, a Gaussian with a width of 5 data points is used and the template size is varied from 25 to 100 min. The double detections in the range where both scales are valid are removed before the statistical evaluation. The distribution of the different templates for the results of the years 2009–2013 is listed in Table 5.1. The different templates used in the algorithm target specific variations

Scales	Template 1	Template 2	Template 3	Template 4	Template 5
5–30 min	2 %	30 %	45 %	8 %	15 %
25– 100 min	3 %	63 %	24 %	4 %	6 %

Table 5.1: Share of templates for all structures in tha data set from 2009–2013.

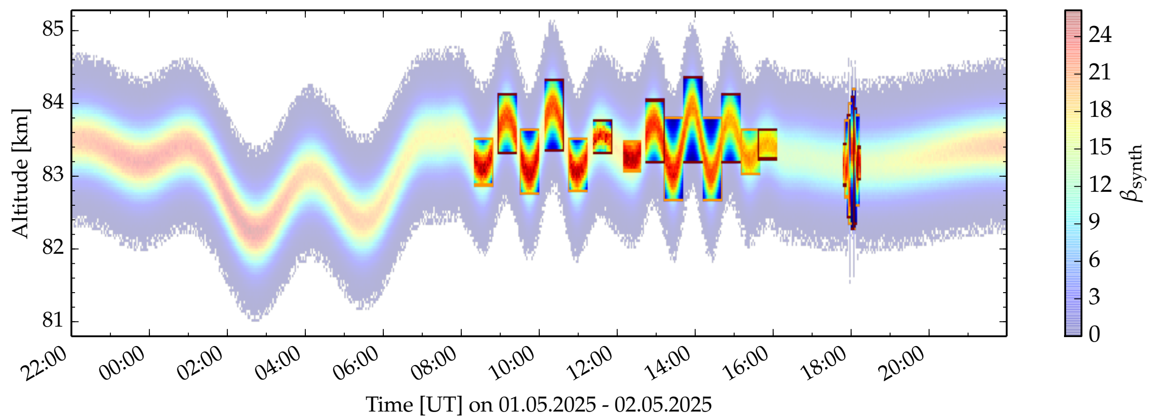

Figure 5.1: Example of a synthetic NLC with the detected structures marked with orange ("V") and red ("Λ") rectangles. The wave with a period of $\sim$ 3 h from 00:00–07:00 is not found by the algorithm, as the templates were limited to a maximum size of 30 minutes. The the other wave events at 10:00, 14:00, and 18:00 are detected.

in the NLC measurements. Template 2 and 3 are found most often, as they target the general characteristic NLC structure. For both scales, they contribute to more than 70 % of the detected matches. The other templates aim to find more specific variations and therefore occur less often. Especially the first template occurs in only 2–3 % of all detected matches.

5.1 Limits of the analysis: synthetic NLC

In a first step, the algorithm is applied to a set of synthetic NLC to document the limits of the method and estimate the uncertainty on the results. The detection algorithm depends on several free parameters, that define the quality of the results. Most importantly, these are the choice of the templates, the threshold value for the detection and the backscatter error and the distance between wave events. The parameters have been optimized using the data subset of 2013, such that the detections of the algorithm correspond best to the visually identifiable wave events. The synthetic data permit to compare the wave events and periods found by the algorithm using these parameters with the simulated wave events. The data set consists of 100 days with 24 h of data, simulating an entire NLC season.

The synthetic NLC consist of a single layer with a Gaussian vertical brightness profile, forming a constant layer width of about 2 km. The height of the layer is modulated by a linear combination of 7 sine waves with different periods. The largest 3 periods in the altitude variations are constant and set to 24, 12 and 8 h, and simulate, with variations in the brightness, the tides in NLC using the parameters from *Fiedler et al.* (2011). These periods are far outside the range of periods targeted by the analysis and are included only to create a natural variation of the NLC layer. The four remaining periods are each chosen randomly between 1 min–30 min, 0.5–1 h, 1–1.5 h and 1.5–6 h. Each appearance of the wave is limited to a few oscillations, with the altitude given by a Gaussian. The entire NLC data are overlaid with a random noise. An example of a synthetic NLC with the results of the detection is shown in Figure 5.1.

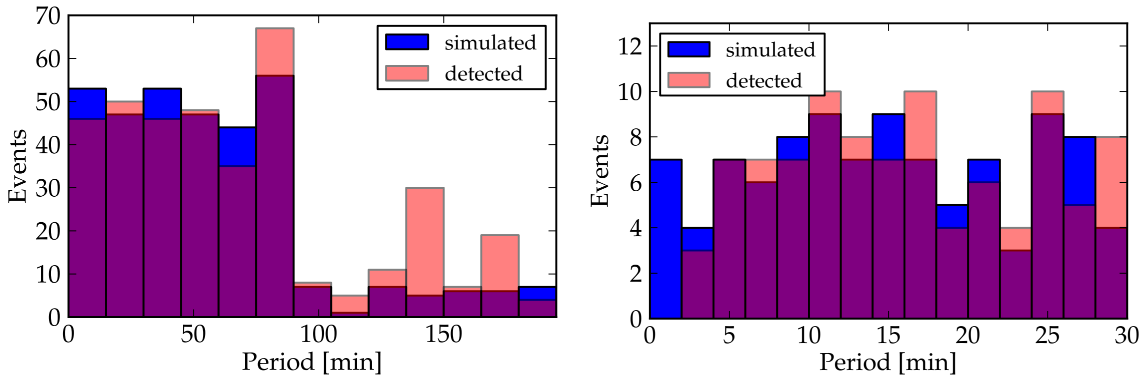

Figure 5.2: Histogram of simulated and detected periods in the synthetic NLC data for periods up to 200 minutes (left) and periods up to 30 minutes (right).

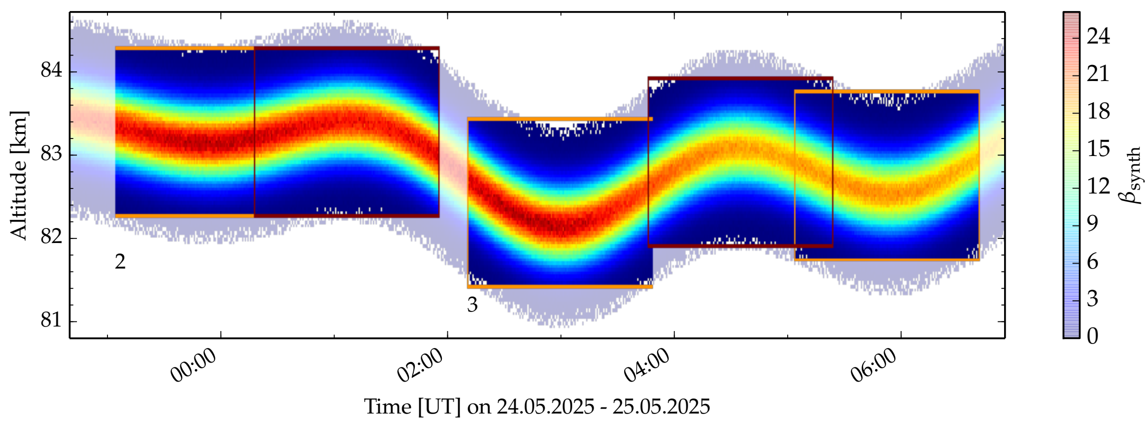

Figure 5.3: Example of a synthetic NLC. The single wave event with a large period is detected as two separate waves, since the distance between the single oscillations is too large. The numbers indicate the number of single wave structures forming the detected wave patterns.

The simulated data do not take into account the varied appearances of the waves in NLC, that are no simple sinusoidal waves, but more complex structures with varying layer width or period during one wave event. Neither gaps in the data nor double layers are included in the simulation, since its objective is in a first place to test the detection probability and the error on the period of the analysis. Figure 5.2 shows the histogram of the detected and the simulated wave events up to 200 min. Up to a period of 100 min, the number of detected waves correspond well to the number of simulated waves. From 100 to 180 min, the number of detected waves is much higher, only for the highest periods from 180 to 200 min, less waves are detected than simulated. When considering only the small periods up to 30 min, a decrease for periods smaller than 5 min is visible. No waves are detected for periods of 2 min or less.

The high number of detections for large periods is explained by a too large distance between the single detections. As shown in Figure 5.3, all single oscillations of the wave are detected. However, because of the underlying low-frequency modulation, the distance be-

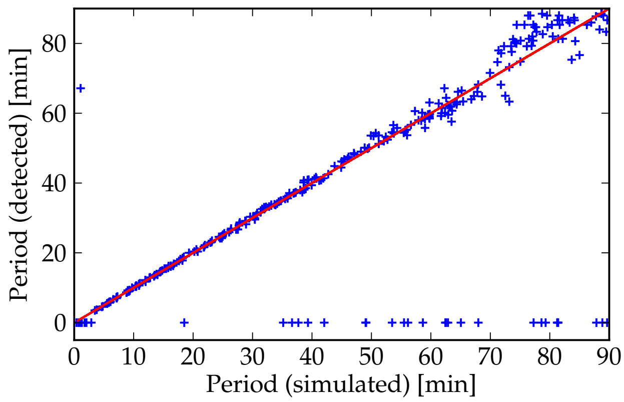

Figure 5.4: Comparison of the simulated period with the period determined by the analysis of the synthetic NLC data.

tween them becomes so large that they are not recognized as a single wave event. Most simulated waves with similar periods are detected more than once, resulting in a surplus of detected waves. For periods near 200 min, for most structures no adjacent variation is found. Since the Lomb-Scargle analysis for the period determination only takes into account wave patterns with at least two detections, the number decreases for waves with these periods.

The differences in the number of detected and simulated small scale (< 90 min) events can be investigated by looking at a direct comparison of the simulated and the detected period in Figure 5.4. The periods for each detected wave is compared with the corresponding simulated period to estimate the error in the period. If a simulated wave event was not detected, the period is shown as 0 in Figure 5.4. In this period range, almost all simulated waves are detected and for periods below 1 h, the difference between the detected period and the simulated period is very small. Around 80 min, the detected period is systematically higher than the simulated period. This explains the difference seen in the histogram, where around 80 min too many waves are detected, while too little are detected in the smaller scale bin. The differences in the histogram therefore are caused by small (< 10 %) uncertainties in the derived period. Considering small periods, the detection successfully recognizes the waves and determines the correct period down to a period of 3 min. Below 3 min, no periods are detected, which corresponds to the decrease seen in the histogram. This lower limit is imposed by the pattern recognition, that sets the minimum size of the template to 5 min to assure a robust distinction between the noise and the visible structures.

For periods > 30 min, the occasional detected period of 0 indicates that a simulated wave event was not found. When the distance between two simulated waves is small, the last oscillation of the first wave and the first oscillation of the second wave may be detected as adjacent structures, resulting in a single, long wave event. The example shown in Figure 5.5 shows that the variations indeed appear as a single wave. Therefore, this effect is intended, as the objective is to recognize such structures of continuous oscillations as one wave events.

The overall good agreement of the results and the simulation shows that the analysis is working as intended. Especially for the small scale structures below 1 hour, which are targeted by the algorithm, the detection probability is high and the error on the period very small. The main results of the data analysis algorithm therefore could be verified by the

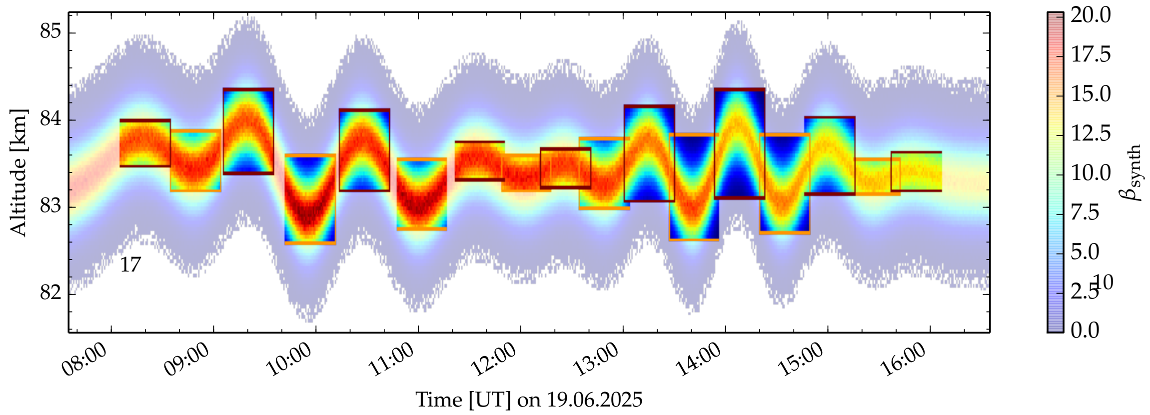

Figure 5.5: Example of two simulated wave events in a synthetic NLC. The two waves slightly overlap, resulting in the detection of a single wave. The number indicates the 17 single variations that form the wave event.

Scale	Single detections	Wave patterns	Lomb-Scargle	Period [min]
5–30 min	4069	1657	854	16 ± 10
25–100 min	1331	514	292	54 ± 30
Combined			1068	26 ± 24

Table 5.2: Number of the single detected wave segments, the resulting wave events, and the wave events for which a Lomb-Scargle periodogram was computed, with the corresponding mean period and standard deviation, for the years 2009–2013, listed for both small and large scales, as well as the final combined results.

use of synthetic data. However, the simulated NLC cannot be considered the same as the complex, real measurement data. This introduces an additional error. The results with the synthetic NLC only give an estimate of the quality and the limits of the algorithm.

5.2 Periods found in NLC

From 2009 to 2013, a total of 4069 short and 1331 long structures ("V" and "Λ") have been detected. As described in Section 4.4, the single detections were combined to 1657 and 514 continuous wave patterns for short and long structures, respectively. About half of the wave events consist of more than one single structure, allowing a Lomb-Scargle frequency analysis. When excluding the wave patterns that are detected twice, 1068 wave events where the period was determined remain (Table 5.2). The amount of detected waves clearly demonstrate the benefit of the algorithm. The alternative to identify each wave pattern visually over this data set alone requires considerable efforts. With the algorithm, the analysis can easily be expanded to include other years or other features, as for example overturning waves.

Figure 5.6 shows the distribution of all periods and for periods below 1 hour. Periods

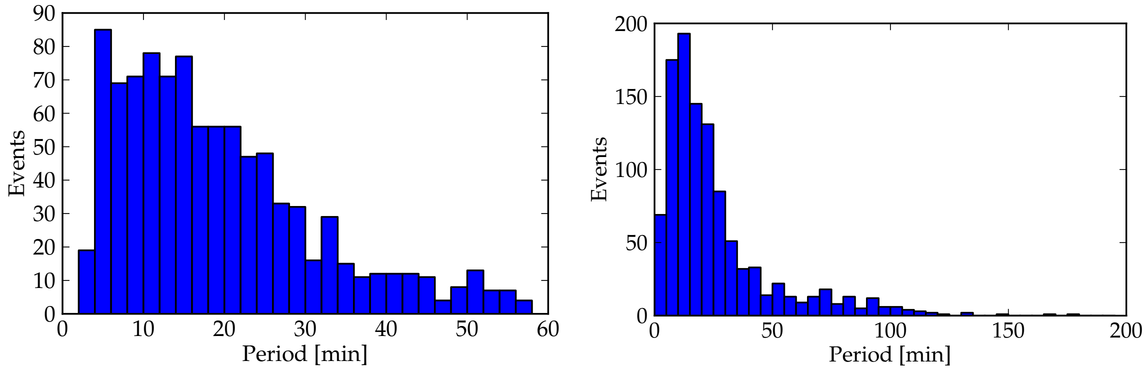

Figure 5.6: Histogram of the periods of the 1068 detected wave events in the NLC data from 2009–2013. In the left figure, only the periods up to 1 h are shown, in the right figure, all periods up to 200 min.

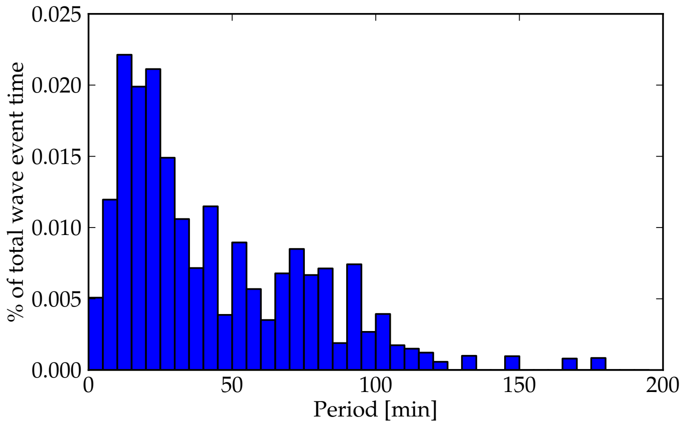

Figure 5.7: Normalized histogram of detected periods weighted with the duration of the wave pattern. This corresponds to the percentage of time for each period in the total time of all detected wave events.

from 5 to 20 min are most frequent and the occurrence rate decreases towards higher periods. From 50–100 min the number of detected events decreases only slightly. Periods larger than 100 min are found only rarely and no period is larger than 180 min.

The results from the synthetic NLC have shown that the notion of “wave event” may lead to erroneous results, if the pattern is not clearly delimited. To circumvent this source of error, it is possible to consider the total duration that waves of a given period are detected. Each detected wave event is therefore weighted with its duration, resulting in the total time that a certain period appears in the data set. The occurrence of the periods in terms of percentage of the total time of all detections is shown in Figure 5.7. This representation also balances the higher possible occurrence of short variations compared to long variations in an NLC segment of a given length. Again periods from 10 to 20 min are most prominent, but longer period (> 50 min) are enhanced compared to Figure 5.6. This shows that indeed periods between 5 and 20 min are most frequent in NLC.

Scale	Events	Wavelength [km]
5–30 min	759	41 ± 30
25–100 min	292	125 ± 90
Combined	973	64 ± 67

Table 5.3: Number of events where the background wind was available and the mean wavelength with standard deviation for small and large scales as well as the combined results.

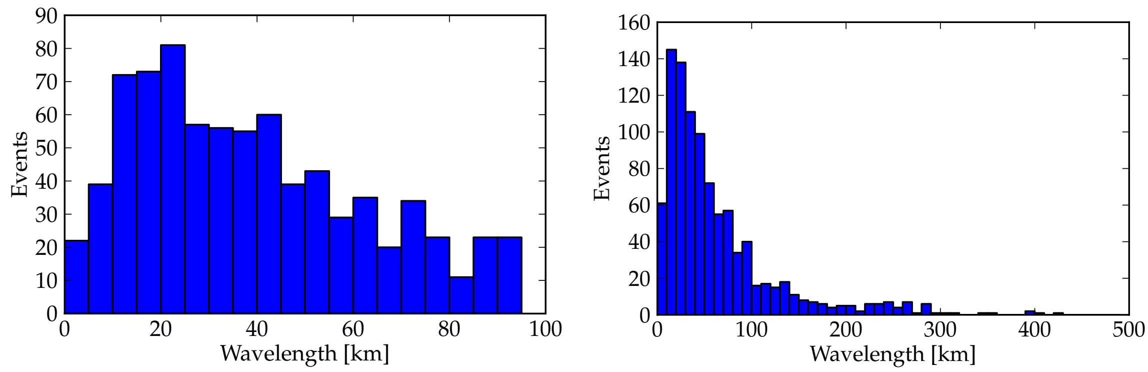

Figure 5.8: Histogram of the wavelengths for the 973 wave events, where the background wind allowed the computation of the wavelength based on the period. In the left figure, only wavelenghts < 100 km are shown, in the right figure, all results for wavelengths up to 500 km.

5.3 Approximate wavelengths in NLC

From the spectral analysis of the wave pattern, an estimate of the period and the wavelength was computed using the background wind from the Saura MF radar as described in Section 4.6. The number of wave events, for which the wavelength could be calculated, is slightly lower, since for some cases no wind data is available. The mean values and standard deviations for the the wavelength are listed in Table 5.3.

The distribution of wavelengths is shown in Figure 5.8. The overall shape of the distribution is similar to the distribution of the periods, with the maximum at 20 km. Most wavelengths are found between 15 and 50 km, but single wavelengths are found up to 430 km. However, it is more likely that these results are outside the range, where the assumptions made for the conversion from period to wavelength are valid. For periods longer than 1 h, it becomes increasingly unlikely that the NLC can be considered as a passive tracer. Over such time scales, it is probable that the shape of the NLC changes while it is moved through the measurement volume. Figure 5.9 therefore shows the wavelengths, separated according to the period from which they are derived. Below 100 km, almost no wavelength is based on a period > 1 h, while almost all wavelengths larger than 200 km might be affected by microphysical changes in the NLC.

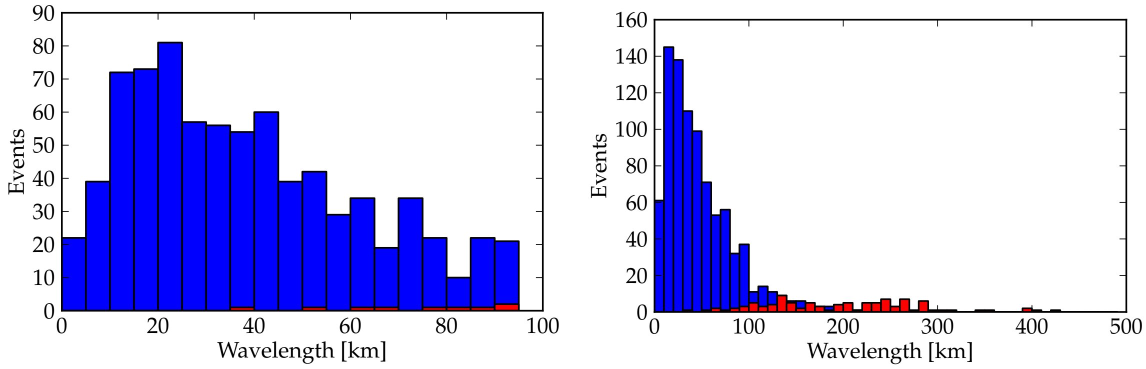

Figure 5.9: Histogram of the wavelengths, separated according to the period of the variation. Wavelengths based on periods $< 1\,\text{h}$ are plotted in blue and wavelengths based on periods $\geq 1\,\text{h}$ are plotted in red. The former variations are on time scales where the conversion might no longer be valid.

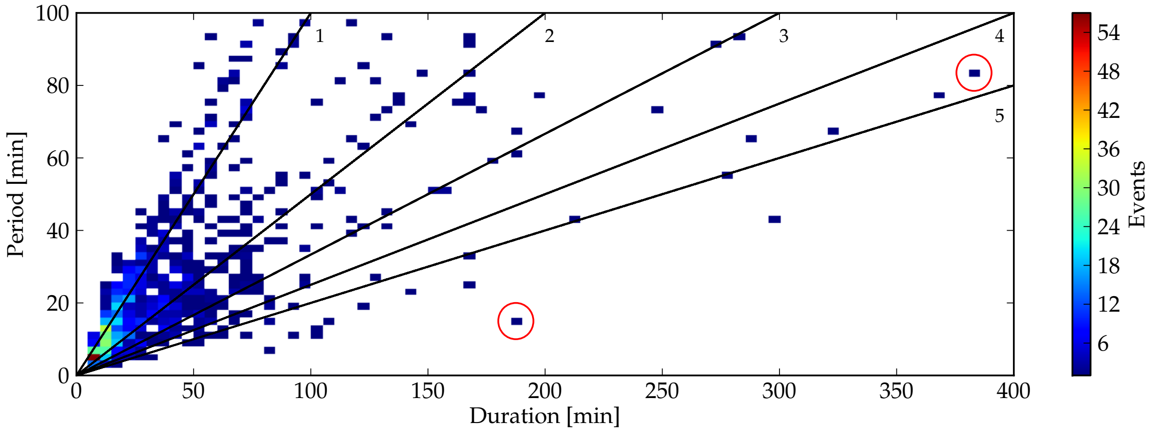

Figure 5.10: 2-d histogram of detected periods plotted against the duration of the wave events. The lines indicate the number of cycles. The highlighted event are shown in Figure 5.11 and Figure 5.12.

5.4 Duration of wave signatures

The period of each wave event can also be compared to the duration, or the number of oscillations, of the pattern in the NLC. This may give an idea of the propagation of the waves through the NLC layer. A wave event extending over several hours is an indication for a horizontally propagating wave, while waves that appear only for a few oscillations in the NLC might be propagating upwards at a steep angle.

Figure 5.10 shows the period of the detected wave events plotted against their duration. It is limited to a period of 100 min, containing the large majority of the detected waves. For most events, the duration is larger than the period, since at least two adjacent structures are required for the computation of the period. If those two structures mostly overlap, the period determined by the periodogram might still be larger than the duration of the whole event.

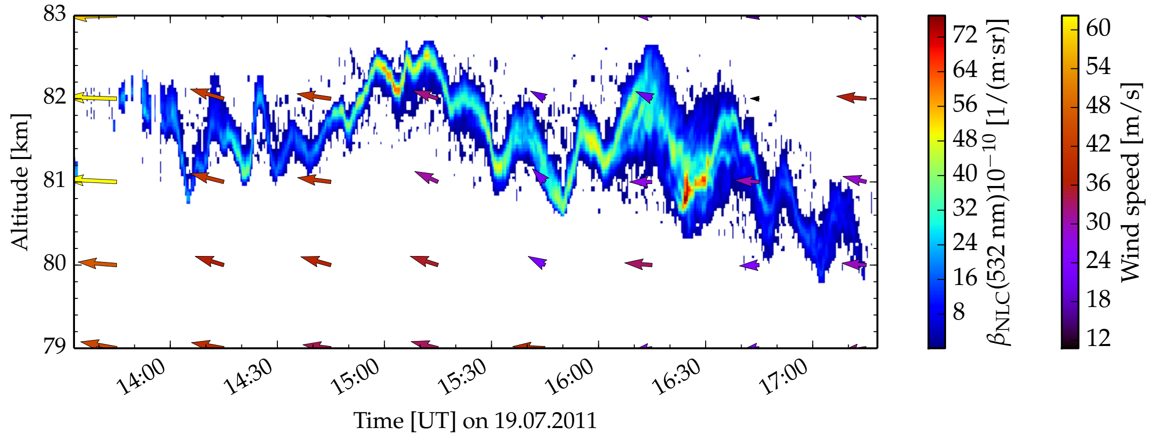

Figure 5.11: NLC on 19. July 2011 with small scale variations extending over 3 h (Event highlighted in Figure 5.10). The arrows indicate the wind direction and speed from the Saura MF radar.

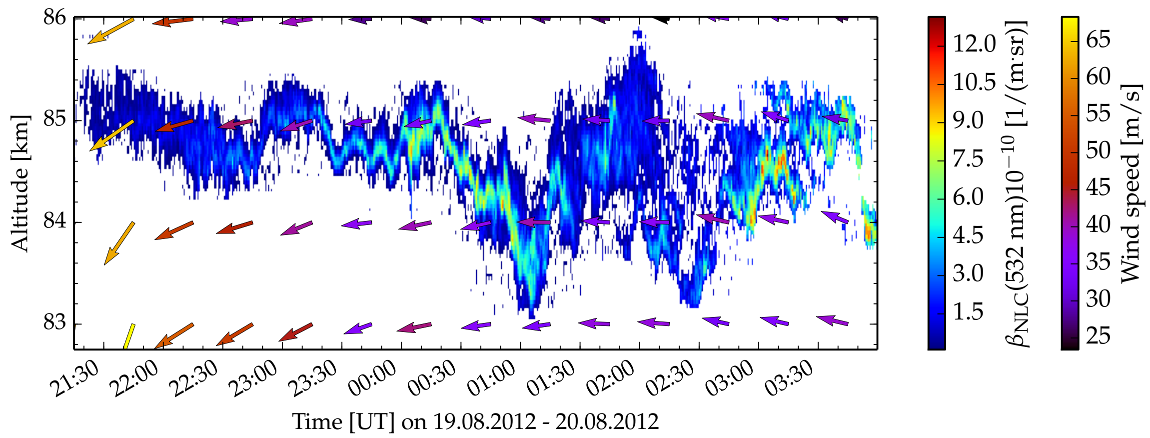

Figure 5.12: NLC on 19. August 2012 with large scale variations and small scale fluctuations extending over 6 h (event highlighted in Figure 5.10). The arrows indicate the wind direction and speed from the Saura MF radar.

For short periods (< 1 h), the majority of wave events lasts for only a few oscillations. The duration of the events is more evenly distributed for the longer periods. For all periods, there are single events that last much longer than one period. An example is shown in Figure 5.11, where a wave extends for over 3 h with a period of about 15 min, thus featuring around 12 periods. Such a number of consecutive variations is only possible for small periods, as the length of the continuous NLC measurements rarely reaches equivalent lengths for large periods. Even the longest events of about 380 min with a period of 80 min, shown in Figure 5.12, still yields “only” 4 oscillations.

6 Discussion

6.1 Limits and uncertainties

Based on the results from the synthetic NLC, the limits of the analysis and the uncertainties of the results are estimated. The period is the direct result of the analysis and is limited by the capabilities of the detection algorithm. The wavelength derived from the period adds an additional error and has a physical meaning only for short periods.

Short period limit

The periods are limited towards smaller periods by the resolution of the data. With a temporal resolution of 30 s and with a minimum of 10 points required to reliably distinguish between noise and a single oscillation, the minimum size of the template is set to 5 min. Periods below 5 min exist and can be found by the pattern recognition, if the limit of 5 min is lowered. However, in this case too many false detections occur, resulting in structures where no wave pattern is visually distinguishable. Figure 6.1 shows an example of detections with the minimum template size set to 3 min. Besides the significant wave patterns, variations in the noisy data are detected.

Variations just below 5 min may still be found, if the correlation with the template is high enough. The correct period is determined by the Lomb-Scargle periodogram. With this limit, only smaller structures that are very clear are detected. This is the case for the

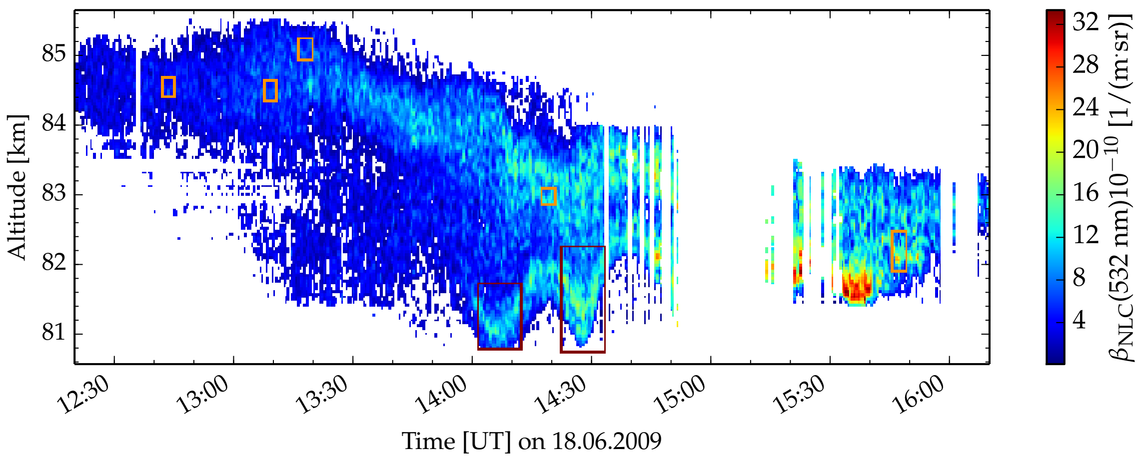

Figure 6.1: Example for false detections in a weak NLC. Variations where the template size is $\geq$ 5 min are marked in red, smaller template sizes are marked in orange. Gaps in the measurement are indicated by missing values over the entire altitude range.

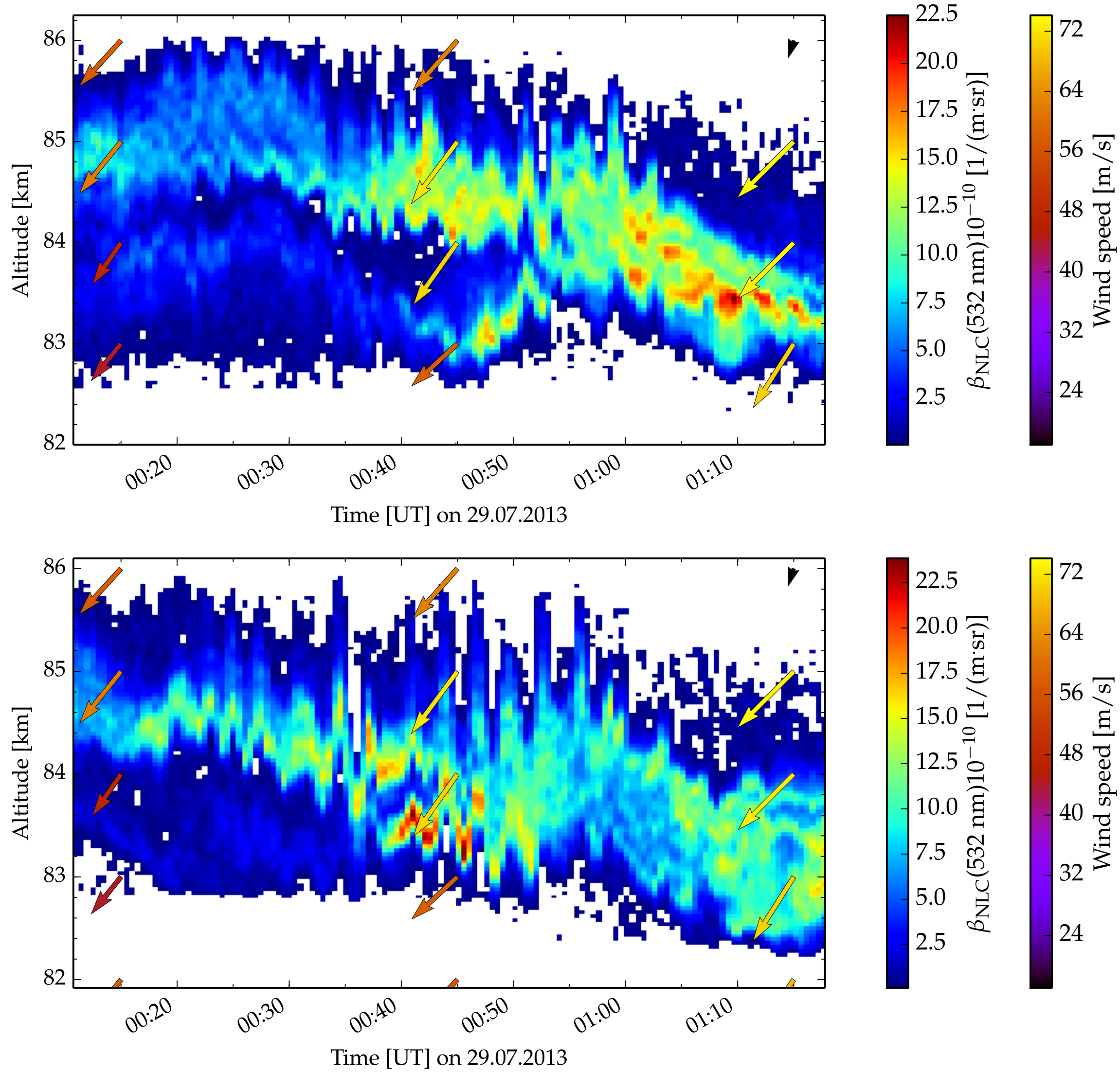

Figure 6.2: NLC on 29. July 2013, measured in northward (upper panel) and eastward (lower panel) direction. Between 00:20 and 01:00 very short variations with a period of only ∼3 minutes are visible, that are not found by the detection algorithm. The arrows indicate the wind speed and direction of the background wind measured by the Saura MF radar.

synthetic NLC data, where variations with periods as low as 3 min are reliably detected. However, examples of real NLC data show that periods as short as 3 min exist, but may not be detected with these parameters, even if they are evident visually. Shown in Figure 6.2 is the observation of an NLC where the telescopes were tilted northwards and eastwards, respectively, resulting in measurement volumes separated by 43 km. In both systems, very short periods < 5 min were observed for 1 h.

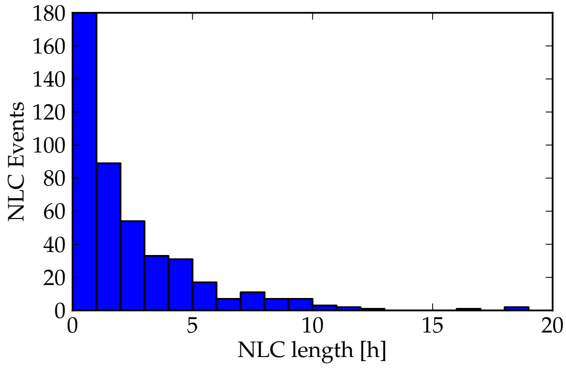

Figure 6.3: Distribution of NLC segment length with maximum gap of 1 h. Only in very few cases continuous NLC over 5 h were measured.

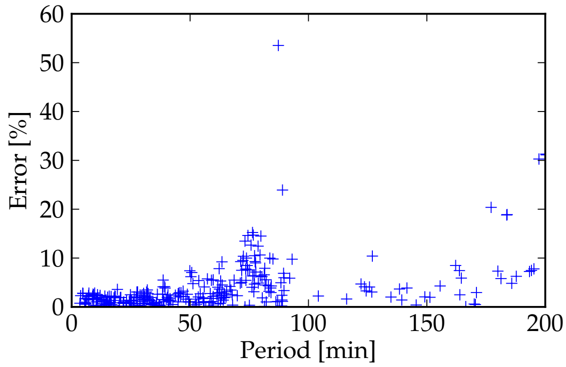

Figure 6.4: Relative error of the measured period based on the results from the synthetic NLC.

Long period limit

The limit is less clearly defined when considering longer periods. The longest structure searched for is 100 min, which sets the theoretical maximum period to 200 min. The synthetic NLC show that for periods longer than 200 min, the distance between two detected oscillations becomes too large, such that they will not be recognized as continuous wave, which prevents a meaningful computation of the periodogram and the length of wave events. The largest period found in the NLC data set is 180 min.

Obviously the upper limit for the period is also determined by the length of the measurement. The data analysis focuses on small variations, therefore the NLC are split into separate events when the gaps in the data are longer than 1 h. The length of the resulting NLC segments limits the length of the periods that can be found. The distribution shown in Figure 6.3 of the length of NLC measurement segments with a mean length of 2.4 h justifies the limit of 3 h set to the detection algorithm. The decrease towards longer periods is at least partly due to the limited length of continuous NLC measurements.

The uncertainty on the detected period can be evaluated using the results from the synthetic data. For all wave events that were detected, the relative error is computed from the difference in the detected and the simulated period (Figure 6.4). For periods < 1 h, which

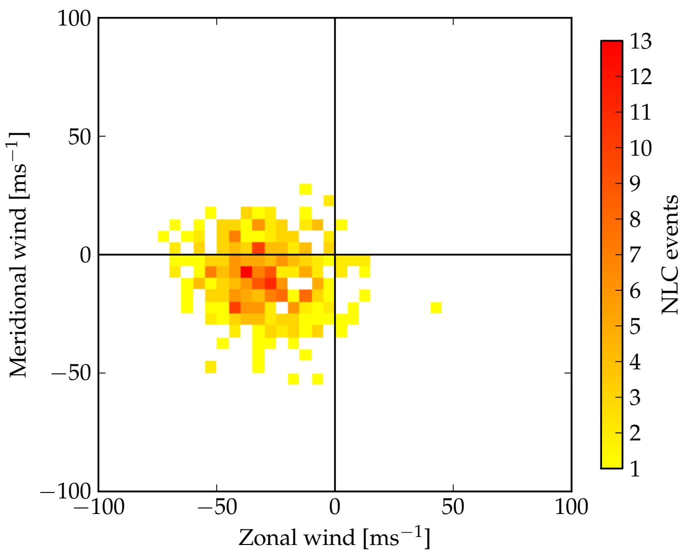

Figure 6.5: Distribution of the mean wind derived by the Saura MF radar during 947 h of NLC events in the years 2009–2013.

make up the majority of the results, the relative error is almost always below 5 %. Only for larger periods it increases, but is in average $< 10\,\%$.

Wavelength

The wavelength is computed from the period and the background wind, which introduces a further error. The simple conversion from period into wavelength with the background wind speed assumes that the wave fronts are oriented orthogonal to the wind (Figure 4.15). Only in this case, the measured wavelength corresponds to the true wavelength, in all other cases it is overestimated. This error cannot be quantified and removed without the knowledge of the propagation direction of the waves, that cannot be obtained from the lidar data. In NLC observations with cameras from Trondheim and Stockholm, most waves had a propagation direction to the north or the north-east (*Pautet et al.*, 2011; *Demissie et al.*, 2014). The wind direction during the NLC events measured at ALOMAR is shown in Figure 6.5. With mean components of $-30\,\mathrm{ms}^{-1}$ in zonal and $-9.5\,\mathrm{ms}^{-1}$ in meridional direction, the wind is predominantly south-westward. The waves seem to propagate against the background flow (*Baumgarten et al.*, 2009), which may add an additional error on the wavelength calculation that assumes pure advection of the wave structures. However, the wavefronts should then be approximately orthogonal to the wind direction, such that the computed wavelength should indeed be close to the actual horizontal wavelength of the waves in the NLC.

Both, wavelength and period, always include the uncertainty, that the lidar does not permit to distinguish between both quantities: The variations that are seen in the lidar data can be either temporal changes that occur while the NLC is in the measurement volume of the laser beam, or spatial variations that appear as variations with time when the NLC is moved through the laser beam by the wind.

Microphysical changes in the NLC can also create the wave structures detected by the lidar in case of brightness fluctuations. The growth or sublimation of particles is a slow process and can be neglected on the time scales of the measurement of the small scale variations (*Kiliani et al.*, 2013). On the other hand, changes in the particle density by the variations in the wind by gravity waves may significantly alter the appearance of the NLC during the measurement. If the NLC would stay immobile during the measurement of one period, this period would indeed correspond to the "true" period of the wave.

The other possibility is an NLC that does not change at all from a microphysical point of view during the measurement of one period. The changes measured by the laser then result only from the advection of the static NLC through the measurement volume of the lidar. The NLC can then be considered as a passive tracer, that might be moved up or down by the vertical wind perturbations caused by gravity waves. In this case, the measured period can be converted to a wavelength using the background wind at the same height and position as the lidar measurement volume.

Using data only from lidar measurements, it is impossible to separate the two scenarios. Comparison of lidar and satellite data showed a good agreement for ± 30 min around a coincident measurement (*Baumgarten et al.*, 2012). A limit of 1 h can therefore be assumed as the time range, where the NLC can be considered as a passive tracer and where the period can be converted into a wavelength using the background wind. This period range includes the majority of the waves up to 100 km in this analysis, therefore the wavelength is assumed to be a valid quantity in this range. Still this time range is only an estimate but one can assume that the uncertainty increases for longer wavelengths.

6.2 Comparison to other gravity wave observations in the mesopause region

NLC camera observations

The small scale variations in the mesopause region can be observed with other instruments than the lidar. With ground based photography of NLC, the wave structures in the brightness can be detected on scales of only a few kilometers. In camera observations of a single event, different wave features with small wavelengths of 4 km and larger wavelengths up to 47 km were detected (*Dalin et al.*, 2004). Systematic evaluation of camera data at Stockholm for small scales has been done by *Pautet et al.* (2011). For 32 wave observations, they found a mean wavelength of 25.1 km, with 60 % of the wavelengths between 20 and 30 km. A comparable study was done for NLC observations from Trondheim by *Demissie et al.* (2014) with very similar results of an average wavelength of 24 km and most wavelengths smaller than 35 km. A comparison with the results from the ALOMAR RMR lidar is shown in Figure 6.6.

The results of the camera images correspond well with the results from the lidar data. For both data sets, most wavelengths are found around 20 km. However, the number of events towards larger wavelengths decreases faster for the camera observations. The field of view of the camera limits the maximum observable wavelength to less than 100 km (*Pautet et al.*, 2011), explaining the different results for larger wavelengths.

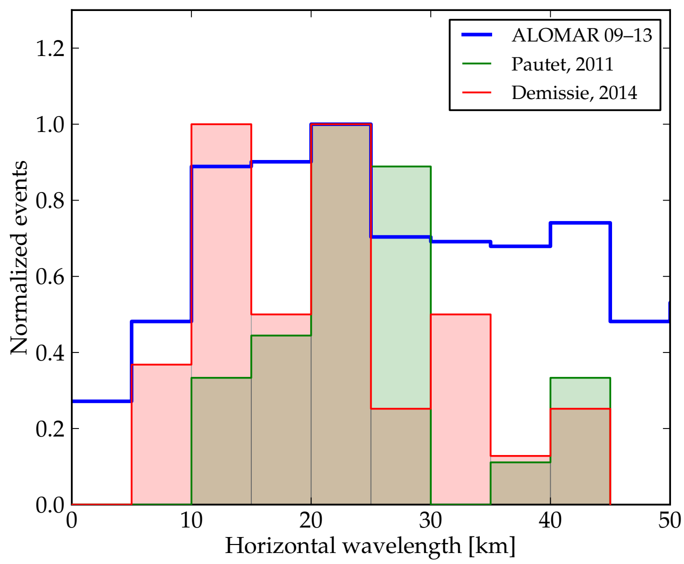

Figure 6.6: Wavelengths from ALOMAR data compared with the results for horizontal wavelengths retrieved from NLC cameras by *Pautet et al.* (2011) and *Demissie et al.* (2014).

NLC satellite observations

NLC images are also taken from space by the Cloud Imaging and Particle Size (CIPS) experiment with a resolution of $\sim$ 5 km (*Lumpe et al.*, 2013). *Chandran et al.* (2009) analyzed the wavelengths visible in the CIPS data for the 2007 season using a wavelet technique, finding that short-period wavelengths were most common. The CIPS data are limited by the size of the NLC images, that extend over approximately 1000 km cross-track and 2000 km along-track for a scene composed of all four camera images. Since the wave events were observed mainly in single images, the maximum wavelength is limited to $\sim$ 350 km. The distribution of wavelength occurrences, shown in Figure 6.7, is very similar for the satellite and the lidar data. In the CIPS data of July 2007, *Taylor et al.* (2011) identified 450 wave events and extracted the wavelengths using an 2-d Fast Fourier Transform. In this analysis, 75% of the waves had wavelengths shorter than 100 km, with the peak around 30–40 km (Figure 6.7). For both analyses of the CIPS dataset, the results show the same peak as observed in the lidar data at small wavelengths.

However, a further analysis of the CIPS data by *Chandran et al.* (2010) attributes this distribution to the manual identification of wave patterns, that favors the visually more apparent small wavelengths. When using a detection algorithm instead, the distribution is shifted to much larger wavelengths, with a peak at a wavelength of 250–300 km (Figure 6.8). This is consistent with the results from *Demissie et al.* (2014), who note that the ray tracing model GROGRAT (*Eckermann and Marks*, 1997) indicates mostly wavelengths larger than 40 km, contrary to the results from the camera observations. Figure 6.8 shows these results compared to the clearly different lidar observations. As discussed in Section 5.1 and 5.3, this difference may be caused by the limits of the analysis of the lidar data. The detection of waves with longer periods is limited by the length of the NLC measurements and the conversion into a wavelength by the microphysical changes in the NLC.

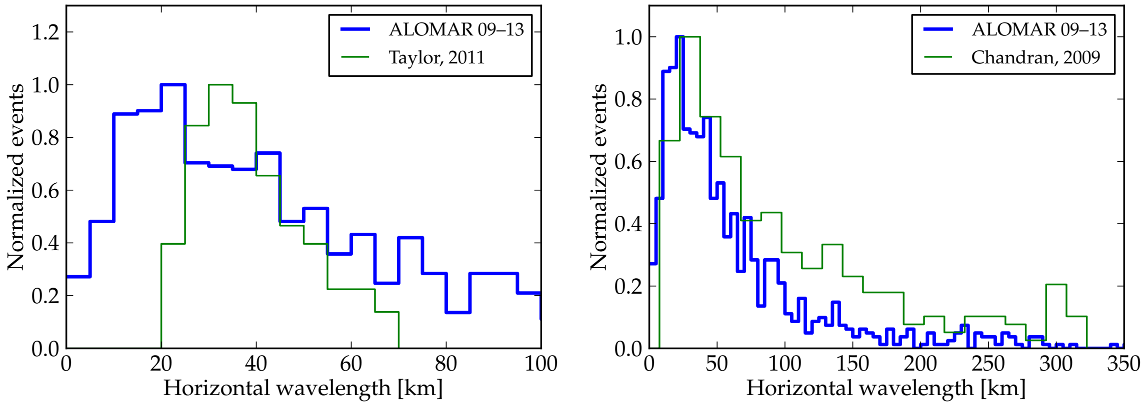

Figure 6.7: ALOMAR wavelengths compared to the wavelengths found by *Taylor et al.* (2011) for small wavelengths (left panel) and by *Chandran et al.* (2009) (right panel) using spaceborne NLC imaging from CIPS on the AIM satellite.

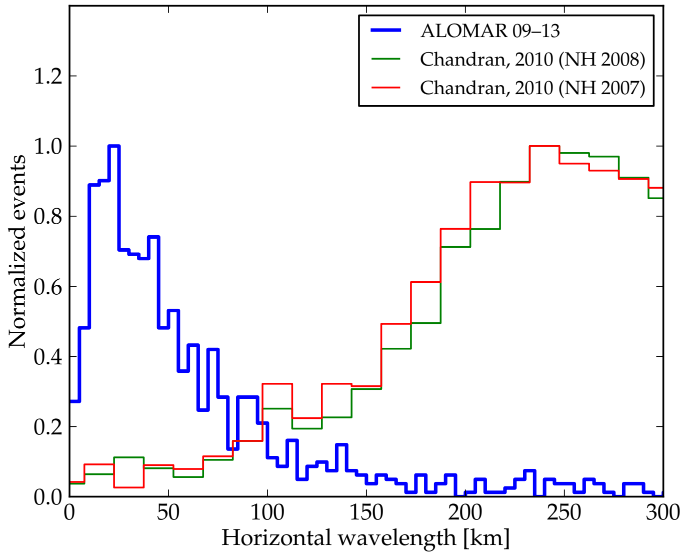

Figure 6.8: Comparison of the ALOMAR data with the results from *Chandran et al.* (2010) for horizontal wavelengths from CIPS. Contrary to *Chandran et al.* (2009) (Figure 6.7), the wave events were identified by an algorithm and not visually, resulting in a different distribution.

Airglow observations

Gravity waves propagating near the mesopause leave a signature not only in NLC, but also in the nearby airglow layer. The airglow is the light emitted by excited atoms in layers at more than 80 km. The lowest layer is created by the infrared emission from the rotational-vibrational states of OH, the OH Meinel bands (*Meinel*, 1950). This layer is centered around 87 km, with a half width of about 8 km (*Baker and Stair*, 1988). While broader than the NLC layer, the airglow layer is in the same altitude range. In the airglow, similar wave structures as in NLC are visible, with horizontal wavelengths from 5 to 100 km (e.g. *Taylor et al.*, 1997). The wavelength and phase speed of the gravity waves in airglow has been studied at dif-

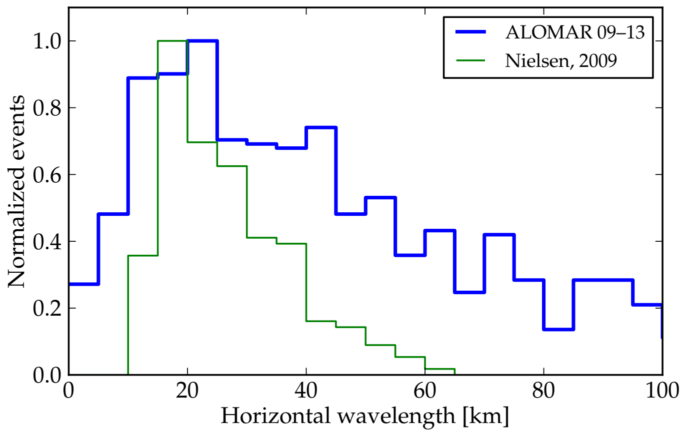

Figure 6.9: Comparison with the results for horizontal wavelengths retrieved from OH airglow imager by *Nielsen et al.* (2009)

ferent locations from low to high latitudes (overview in *Nielsen et al.*, 2009). In Figure 6.9, the lidar results are exemplarily compared to one study of *Nielsen et al.* (2009) in Antarctica during two austral winter seasons, though many other studies at different latitudes with similar results exist. The airglow results have a similar peak wavelength at 20 km, but less events than in the lidar data with a large wavelength are observed. Like for the NLC observations using ground based cameras, the field of view of the airglow imager limits the maximum observable wavelength.

The results for wavelengths obtained from the lidar data correspond to other observations in the same range of observable wavelengths, with all of them finding most wavelengths at 20–30 km. With wavelengths of this order, this corresponds to what is visually observed as bands from the ground and is generated by gravity waves, other than the even smaller billows, that are attributed to shortlived, local instabilities (e.g. *Witt*, 1962; *Fritts et al.*, 1993). From the CIPS satellite studies it can be assumed that the waves with larger wavelengths are also visible in NLC, but are too large to be detected with the data and the algorithm used in this thesis.

Contrary to the other studies, the waves are not identified based on the brightness, but on the variations of the height of the NLC layer. The similar results to the observations of wave events seen in the NLC brightness indicate that these variations are generated by the same process. The passing gravity waves lead to brightness variations by fluctuations of the wind, causing variations in the particle density (*Fritts et al.*, 1993). Similarly, fluctuations of the vertical wind modulate the altitude of the bright NLC layer on small scales, and the distribution of detected wavelengths represents the spectrum of gravity waves propagating in the mesosphere.

6.3 Gravity wave propagation

Besides the period and thereby the wavelength, the duration of each wave event can be extracted from the results of the pattern detection. With the variations caused by gravity waves, the time that their signatures are visible in the NLC is determined by their passage through the NLC layer. Gravity waves propagate horizontally as well as vertically through the atmosphere, influenced by the atmospheric background conditions (*Fritts and Alexander*, 2003). Gravity waves propagating vertically at a steep angle would be visible only for a few oscillations in the narrow NLC layer.

The duration of the individual wave pattern compared to their period shows that indeed most short period waves are seen in the NLC for no longer than once or twice their period. The peak at short wave events is less pronounced for the larger periods, that are more likely to be observed for a longer time span. The few exceptions where a wave of a small wavelength is visible over hours may be caused by a ducted or by an evanescent wave. Ducted and evanescent waves are commonly observed in the OH airglow layer, where the additional information of the phase speed permit to determine the vertical wavenumber of the wave (e.g. *Simkhada et al.*, 2009).

Gravity waves are propagating vertically as long as for the vertical wavenumber m, $m^2 > 0$ (*Isler et al.*, 1997). For high frequency gravity waves, $\omega_\mathrm{I} \gg f$, and the relation for m in equation 2.9 simplifies to

$$m^2 = \frac{N^2}{(c - u_0)^2} - k^{*2} - \frac{1}{4H^2}, \tag{6.1}$$

with the horizontal wavenumber $k^{*2} = k^2 + l^2$ and the observed phase speed c. In regions where $m^2 < 0$, the wave is evanescent and propagates only horizontally, similar to a surface wave. A duct consists of two regions of evanescence, between which the wave is trapped or ducted. Ducting occurs when the background atmosphere changes such that m becomes negative. A Doppler duct is created by the changes in the mean background wind u_0, which changes m. Changes in the temperature create a thermal duct due to the change in the Brunt-Väisälä frequency N. Waves with a small horizontal wavelength are more likely to be ducted (*Fritts and Alexander*, 2003). Wave ducting by either the temperature or the wind can explain the horizontally propagating, quasi-monochromatic waves that are often observed in airglow at a similar height as NLC. It is therefore reasonably to assume that similar wave ducting could be observed in NLC.

The observation of long lasting short scale wave events in NLC may be attributed to vertically trapped waves, either ducted or evanescent (e.g. *Isler et al.*, 1997; *Walterscheid et al.*, 1999). From Figure 5.10 it becomes clear that wave events, that are considerably longer than the wavelength, occur only in a few cases and mostly for small wavelengths. This effect is at least partly caused by the limitation in terms of length of the data, similar to the upper limit to the detected wavelength. The duct may also exist only for a given duration, until the atmospheric conditions change, possibly due to large scale waves or tides (*Bossert et al.*, 2014). Using airglow data, the vertical wave number m can be determined using the horizontal wavelength, the phase speed and the background wind using equation 2.9. This approach is not possible for the lidar data, as it does not provide the necessary information about the phase speed of the wave.

However, the vertical profile of the NLC layer is available from the lidar data, where the vertical propagation of the gravity waves may be observed. A characteristic feature of NLC is their vertical structure that may present multiple brightness maxima. Mostly double layers, but also triple layers can be observed in the brightness profile of the NLC. Figure 6.10

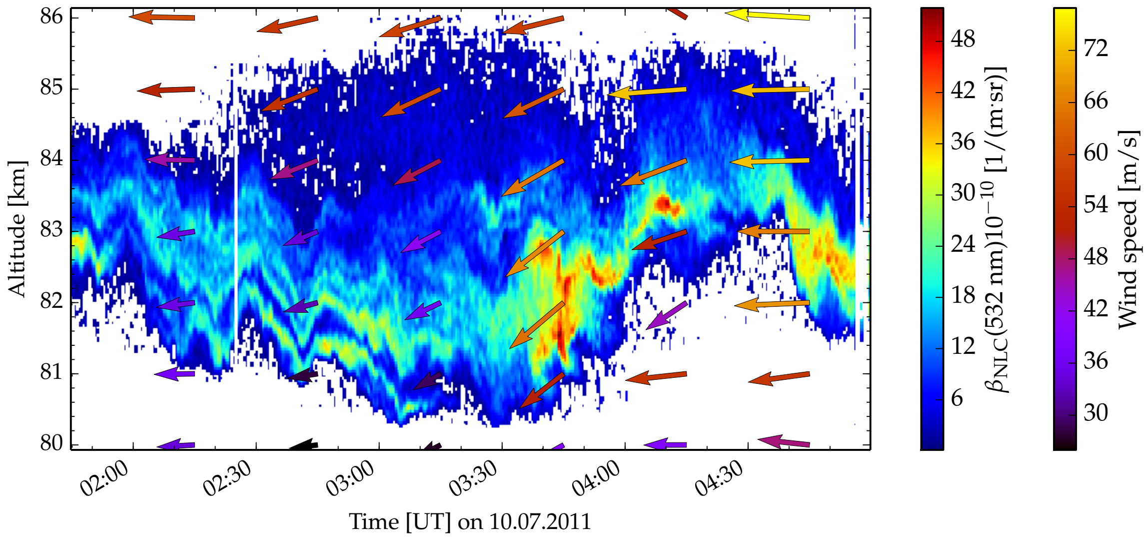

Figure 6.10: Example of an NLC with a large vertical extend > 4 km and with a vertical structure, where around 02:15, 4 layers with a very short vertical distance are visible. In all 4 layers, wave structures are visible. The arrows indicate the wind direction and speed from the Saura MF radar.

shows the rare case of an NLC, where even up to four layers can be distinguished. The layers can be completely separated vertically, or consist of brighter NLC layers, separated by weaker layers. If wavelike features are detected at the same time but at different altitudes, as shown in Figure 6.11, they are considered as multiple layers. From all detected structures, double layers occur in 7.1 % of the detected structures, with a mean vertical distance of 1.0 km. Three layers are detected only in 0.3 % of the variations. *Müller* (2009) found that separated double layers occur in 9.8% and triple layers in 0.8 % of the observed NLC, with a mean vertical distance of 1.63 ± 0.91 km. When defining layers as brightness maximum with a decrease of brightness under a certain threshold, 7.9 % up to 33.8 % of NLC present multiple layers, depending on the threshold (*Kaifler et al.*, 2013). This definition is closer to the understanding of multiple layers used here. The rate of multiple layers is slightly higher, but may depend on the data set and the threshold value. The vertical distance is smaller, which might be due to the different definition of multiple layers, that does not require the NLC to be separated vertically. Geophysically, multiple layers are a signature of the vertical propagation of small scale gravity waves that modulate the vertical brightness profile of the NLC. They might be used as an indication for the vertical wavelength of the gravity waves propagating in the mesopause region.

Besides the previously presented results, more information about the variations in the NLC layer can be extracted from the detected patterns. The separation of the NLC in structured and unstructured parts allows to characterize the amount of waves in the NLC. Normalized to the duration of the NLC measurements, this can be used as a measure of the gravity wave activity.

Gravity waves influence the growth and the sublimation of particles in the NLC by the induced temperature variations. Model simulations have shown that gravity waves with

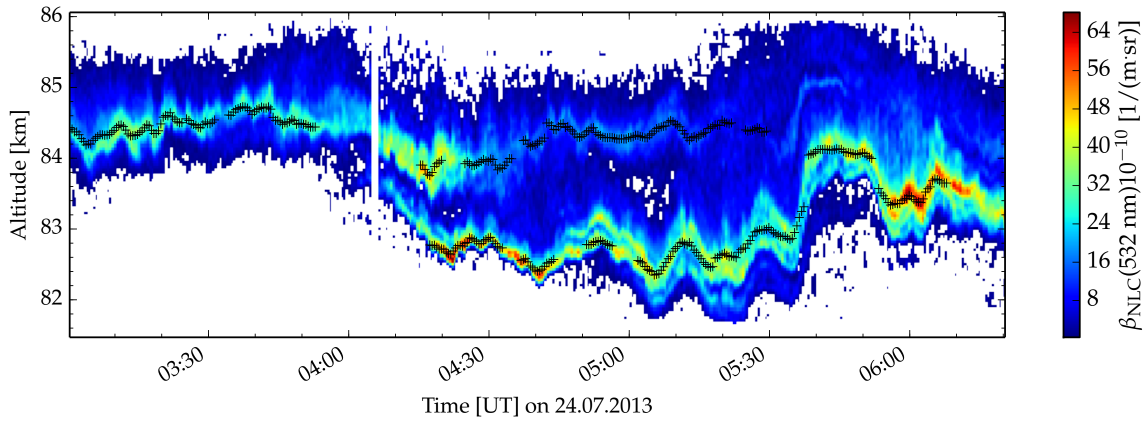

Figure 6.11: NLC with the centroid altitude of the identified wave structures (black). A double layer appears at 04:00–05:50 with a vertical distance of $\sim$ 1–1.5 km.

periods longer than 6.5 h tend to enhance NLC, while shorter periods destroy them (*Rapp and Thomas*, 2006). Many studies have searched for evidence of this relationship in NLC data, with different results, depending on the location (e.g. *Thayer et al.*, 2003; *Chu et al.*, 2009; *Wilms et al.*, 2013). To characterize the wave activity, the background wind either in the stratosphere or at the height of the NLC is considered. The wave activity based on the waves visible in the NLC might provide a direct measurement of gravity waves that had an effect on the NLC. The periods detected here are far below the critical period of 6.5 h, but still an influence of the wave activity on the brightness, or, more directly, the particle size, may be possible.

7 Conclusion and outlook

The waves observable in the brightness of NLC have been previously studied from the ground or by satellite. To measure such small scale variations with a lidar, a system providing data at a high resolution is necessary. With the temporal and spatial resolution of only 30 s and 40 m respectively, variations of only a few minutes, corresponding to spatial structures of several km, are resolved in the data of the ALOMAR RMR lidar. The short period variations in the height of the NLC layer were extracted from the structured parts of the NLC so that the duration, period, and wavelength of each wave event could be determined.

To analyze the small scale structures visible in almost every cloud, a visual identification of every variation is inefficient and unreliable when considering the large data set. The objective therefore was in a first place to develop an analysis that extracts the small scale wave patterns from the NLC data. The analysis of the synthetic data and visual verification of the results in the measurement data confirms that the detected wave patterns correspond to the expected results.

The pattern recognition is necessary to find the small scale variations that appear only over a short time, maybe only for a single oscillation. With this new algorithm it is possible to find waves at scales that could previously not be resolved by other approaches as Fourier or wavelet analysis. Using the data set of the years 2009–2013, over 1000 wave patterns consisting of several oscillations were found in 947 h of NLC measurements. The statistical evaluation of the period shows a peak in the distribution of the periods at 5–20 min. The horizontal scales were estimated using the background wind measurements from collocated radar instruments. Most wavelengths were found around 10–30 km and only a few are larger than 100 km.

Other studies of wave signatures at mesospheric heights using either observations of NLC or OH airglow find similar distributions with the majority of the wavelengths at $\sim$ 20 km. Only previous studies from satellite data found a maximum also towards 250 km, which might be explained by the global coverage of the data, allowing the analysis of wavelengths outside the scope of the lidar data.

The comparison of the duration of the wave patterns with their period shows that most variations with small periods appear only for a short time, as would be expected from short-period gravity waves propagating mostly vertically. In a few cases, the waves were visible in the NLC layer over hours, which might indicate a gravity wave travelling horizontally, possibly due to ducting, as it is observed frequently in the nearby airglow layer.

The extracted wave patterns can be used for further studies in combination with other data. The microphysical properties of NLC are modified by small scale gravity waves, notably the size of the ice particles. With the activity of waves in the NLC based on the occurrence of variations in the NLC layer, the activity of gravity waves could be compared to the brightness of the NLC, or directly to the particle size.

The amplitude of the variations in the layer can easily be determined from the wave patterns. With the variations created by the wind, this might be used to estimate the vertical wind fluctuations due to gravity waves.

For the results presented here, both systems of the ALOMAR RMR lidar were considered independently. However, the same NLC is measured at different points and a comparison of structures found in both systems can provide a possibility to separate the microphysical changes in the NLC from the changes caused by advection.

Finally, it would be possible to use the pattern detection on other data sets, that present similar structures, like PMSE radar observations. As the shape of the templates can easily be changed, an adaption to slightly different structures is possible. When extending the set of templates used in the pattern recognition, other characteristic structures in NLC or similar data could be extracted.

Bibliography

Backhouse, T. W., The luminous cirrus clouds of June and July, *Meterol. Mag.*, *20*, p. 133, 1885.

Baker, D. J., and A. T. Stair, Jr, Rocket measurements of the altitude distributions of the hydroxyl airglow, *Phys. Scripta*, *37*(4), 611, 1988.

Baumgarten, G., F.-J. Lübken, and K. H. Fricke, First observation of one noctilucent cloud by a twin lidar in two different directions, *Ann. Geophys.*, *20*(11), 1863–1868, doi:10.5194/angeo-20-1863-2002, 2002.

Baumgarten, G., J. Fiedler, K. H. Fricke, M. Gerding, M. Hervig, P. Hoffmann, N. Müller, P.-D. Pautet, M. Rapp, C. Robert, D. Rusch, C. von Savigny, and W. Singer, The noctilucent cloud (NLC) display during the ECOMA/MASS sounding rocket flights on 3 August 2007: morphology on global to local scales, *Ann. Geophys.*, *27*(3), 953–965, doi:10.5194/angeo-27-953-2009, 2009.

Baumgarten, G., A. Chandran, J. Fiedler, P. Hoffmann, N. Kaifler, J. Lumpe, A. Merkel, C. E. Randall, D. Rusch, and G. Thomas, On the horizontal and temporal structure of noctilucent clouds as observed by satellite and lidar at ALOMAR (69N), *Geophys. Res. Lett.*, *39*(1), doi:10.1029/2011GL049935, 2012.

Bossert, K., D. C. Fritts, P.-D. Pautet, M. J. Taylor, B. P. Williams, and W. R. Pendelton, Investigation of a mesospheric gravity wave ducting event using coordinated sodium lidar and Mesospheric Temperature Mapper measurements at ALOMAR, Norway (69°N), *J. Geophys. Res.*, pp. n/a–n/a, doi:10.1002/2014JD021460, 2014.

Chandran, A., D. W. Rusch, S. E. Palo, G. E. Thomas, and M. J. Taylor, Gravity wave observations in the summertime polar mesosphere from the Cloud Imaging and Particle Size (CIPS) experiment on the AIM spacecraft, *J. Atmos. Solar-Terr. Phys.*, *71*(3–4), 392–400, doi:http://dx.doi.org/10.1016/j.jastp.2008.09.041, 2009.

Chandran, A., D. W. Rusch, A. W. Merkel, S. E. Palo, G. E. Thomas, M. J. Taylor, S. M. Bailey, and J. M. Russell III, Polar mesospheric cloud structures observed from the cloud imaging and particle size experiment on the Aeronomy of Ice in the Mesosphere spacecraft: Atmospheric gravity waves as drivers for longitudinal variability in polar mesospheric cloud occurrence, *J. Geophys. Res.*, *115*(D13), n/a–n/a, doi:10.1029/2009JD013185, 2010.

Chu, X., C. Yamashita, P. J. Espy, G. J. Nott, E. J. Jensen, H.-L. Liu, W. Huang, and J. P. Thayer, Responses of polar mesospheric cloud brightness to stratospheric gravity waves at the South Pole and Rothera, Antarctica, *J. Atmos. Solar-Terr. Phys.*, *71*(3–4), 434–445, doi:http://dx.doi.org/10.1016/j.jastp.2008.10.002, 2009.

Dalin, P., S. Kirkwood, A. Moström, K. Stebel, P. Hoffmann, and W. Singer, A case study of gravity waves in noctilucent clouds, *Ann. Geophys.*, *22*(6), 1875–1884, doi:10.5194/angeo-22-1875-2004, 2004.

DeLand, M. T., E. P. Shettle, G. E. Thomas, and J. J. Olivero, Solar backscattered ultraviolet (SBUV) observations of polar mesospheric clouds (PMCs) over two solar cycles, *J. Geophys. Res.*, *108*(D8), doi:10.1029/2002JD002398, 2003.

Demissie, T. D., N. H. Kleinknecht, P. J. Espy, N. Kaifler, and G. Baumgarten, Characteristics and sources of gravity waves observed in NLC over Norway, *Atmos. Chem. Phys. Discuss.*, submitted, 2014.

Donahue, T. M., B. Guenther, and J. E. Blamont, Noctilucent clouds in daytime: circumpolar particulate layers near the summer mesopause, *J. Atmos. Sci.*, *29*, 1205–1209, 1972.

Eckermann, S. D., and C. J. Marks, GROGRAT: A new model of the global propagation and dissipation of atmospheric gravity waves , *Adv. Space Res.*, *20*(6), 1253–1256, doi: http://dx.doi.org/10.1016/S0273-1177(97)00780-1, 1997.

Fiedler, J., and G. Baumgarten, On the relationship between lidar sensitivity and tendencies of geophysical time series, in *Reviewed and Revised Papers at the 26th International Laser Radar Conference, Porto Heli, Greece, 2012*, pp. 63–66, 2012.

Fiedler, J., G. Baumgarten, and G. von Cossart, Mean diurnal variations of noctilucent clouds during 7 years of lidar observations at ALOMAR, *Ann. Geophys.*, *23*(4), 1175–1181, doi:10.5194/angeo-23-1175-2005, 2005.

Fiedler, J., G. Baumgarten, and F.-J. Lübken, NLC observations during one solar cycle above ALOMAR , *J. Atmos. Solar-Terr. Phys.*, *71*(3–4), 424 – 433, doi:http://dx.doi.org/10.1016/j.jastp.2008.11.010, 2009.

Fiedler, J., G. Baumgarten, U. Berger, P. Hoffmann, N. Kaifler, and F.-J. Lübken, NLC and the background atmosphere above ALOMAR, *Atmos. Chem. Phys.*, *11*(12), 5701–5717, doi: 10.5194/acp-11-5701-2011, 2011.

Fiedler, J., G. Baumgarten, U. Berger, A. Gabriel, R. Latteck, and F.-J. Lübken, On the early onset of the NLC season 2013 as observed at ALOMAR, *J. Atmos. Solar-Terr. Phys.*, in print, 2014.

Fleming, E. L., S. Chandra, J. J. Barnett, and M. Corney, Zonal mean temperature, pressure, zonal wind, and geopotential height as functions of latitude, COSPAR International Reference Atmosphere: 1986, Part II: Middle Atmosphere Models, *Adv. Space Res.*, *10*(12), 11–59, 1990.

Fritts, D. C., and M. J. Alexander, Gravity wave dynamics and effects in the middle atmosphere, *Rev. Geophys.*, *41*(1), doi:10.1029/2001RG000106, 2003.

Fritts, D. C., J. R. Isler, G. E. Thomas, and O. Andreassen, Wave breaking signatures in noctilucent clouds, *Geophys. Res. Lett.*, *20*(19), 2039–2042, doi:10.1029/93GL01982, 1993.

Gadsden, M., and W. Schröder, *Noctilucent clouds*, *Physics and chemistry in space – Planetology*, vol. 18, 165 pp., Springer-Verlag, New York, 1989.

Geller, M. A., Dynamics of the middle atmosphere, *Space Sci. Rev.*, *34*(4), 359–375, doi:10.1007/BF00168828, 1983.

Hansen, G., M. Serwazi, and U. von Zahn, First detection of a noctilucent cloud by lidar, *Geophys. Res. Lett.*, *16*(12), 1445–1448, doi:10.1029/GL016i012p01445, 1989.

Hervig, M., R. E. Thompson, M. McHugh, L. L. Gordley, J. M. Russell III, and M. E. Summers, First confirmation that water ice is the primary component of polar mesospheric clouds, *Geophys. Res. Lett.*, *28*(6), 971–974, doi:10.1029/2000GL012104, 2001.

Höffner, J., and F.-J. Lübken, Potassium lidar temperatures and densities in the mesopause region at Spitsbergen (78° N), *J. Geophys. Res.*, *112*(D20), D20114, doi:10.1029/2007JD008612, 2007.

Holton, J. R., The Influence of Gravity Wave Breaking on the General Circulation of the Middle Atmosphere, *J. Atmos. Sci.*, *40*, 2497–2507, doi:10.1175/1520-0469(1983)040⟨2497:TIOGWB⟩2.0.CO;2, 1983.

Isler, J. R., M. J. Taylor, and D. C. Fritts, Observational evidence of wave ducting and evanescence in the mesosphere, *J. Geophys. Res.*, *102*(D22), 26,301–26,313, doi:10.1029/97JD01783, 1997.

Jensen, E. J., and G. E. Thomas, Numerical simulations of the effects of gravity waves on noctilucent clouds, *J. Geophys. Res.*, *99*(D2), 3421–3430, doi:10.1029/93JD01736, 1994.

Jesse, O., Auffallende Abenderscheinungen am Himmel, *Meteorol. Z.*, *2*, 311–312, 1885.

Jesse, O., Die Höhe der leuchtenden Nachtwolken, *Astr. Nach.*, *140*(11), 161–168, doi:10.1002/asna.18961401102, 1896.

Kaifler, N., G. Baumgarten, J. Fiedler, R. Latteck, F.-J. Lübken, and M. Rapp, Coincident measurements of PMSE and NLC above ALOMAR (69° N, 16° E) by Radar and Lidar from 1999-2008, *Atmos. Chem. Phys.*, doi:10.5194/acpd-11-1355-2011, 2011.

Kaifler, N., G. Baumgarten, J. Fiedler, and F.-J. Lübken, Quantification of waves in lidar observations of noctilucent clouds at scales from seconds to minutes, *Atmos. Chem. Phys.*, *13*(23), 11,757–11,768, doi:10.5194/acp-13-11757-2013, 2013.

Kiliani, J., G. Baumgarten, F.-J. Lübken, U. Berger, and P. Hoffmann, Temporal and spatial characteristics of the formation of strong noctilucent clouds, *J. Atmos. Solar-Terr. Phys.*, *104*, 151–166, doi:10.1016/j.jastp.2013.01.005, 2013.

Leslie, R. C., Sky Glows, *Nature*, *32*, 245, doi:10.1038/032245a0, 1885.

Lindzen, R. S., Turbulence and Stress Owing to Gravity Wave and Tidal Breakdown, *J. Geophys. Res.*, *86*(C10), 9707–9714, 1981.

Lomb, N. R., Least-squares frequency analysis of unequally spaced data, *Astrophys. Space Sci.*, *39*, 447–462, doi:10.1007/BF00648343, 1976.

Lumpe, J. D., S. M. Bailey, J. N. Carstens, C. E. Randall, D. W. Rusch, G. E. Thomas, K. Nielsen, C. Jeppesen, W. E. McClintock, A. W. Merkel, L. Riesberg, B. Templeman, G. Baumgarten, and J. M. Russell III, Retrieval of polar mesospheric cloud properties from CIPS: Algorithm description, error analysis and cloud detection sensitivity, *J. Atmos. Solar-Terr. Phys.*, *104*(0), 167 – 196, doi:http://dx.doi.org/10.1016/j.jastp.2013.06.007, 2013.

Lübken, F.-J., Thermal structure of the Arctic summer mesosphere, *J. Geophys. Res.*, *104*(D8), 9135–9149, doi:10.1029/1999JD900076, 1999.

Meinel, A. B., OH emission bands in the spectrum of the night sky. I, *Am. J. Phys.*, *111*, 555–564, 1950.

Meriwether, J. W., and A. J. Gerrard, Mesosphere inversion layers and stratosphere temperature enhancements, *Rev. Geophys.*, *42*(3), RG3003, doi:10.1029/2003RG000133, 2004.

Müller, N., Beobachtung von Fluktuationen im Minutenbereich in leuchtenden Nachtwolken mit dem ALOMAR RMR-Lidar (69°N), Master's thesis, Universität Heidelberg, 2009.

Nielsen, K., M. J. Taylor, R. E. Hibbins, and M. J. Jarvis, Climatology of short-period mesospheric gravity waves over Halley, Antarctica (76°S, 27°W), *J. Atmos. Solar-Terr. Phys.*, *71*(8–9), 991 – 1000, doi:http://dx.doi.org/10.1016/j.jastp.2009.04.005, 2009.

Nussbaumer, V., K. H. Fricke, M. Langer, W. Singer, and U. von Zahn, First simultaneous and common volume observations of noctilucent clouds and polar mesosphere summer echoes by lidar and radar, *J. Geophys. Res.*, *101*(D14), 19,161–19,167, doi:10.1029/96JD01213, 1996.

Pautet, P.-D., J. Stegman, C. M. Wrasse, K. Nielsen, H. Takahashi, M. J. Taylor, K. W. Hoppel, and S. D. Eckermann, Analysis of gravity waves structures visible in noctilucent cloud images, *J. Atmos. Solar-Terr. Phys.*, *73*(14–15), 2082–2090, doi:http://dx.doi.org/10.1016/j.jastp.2010.06.001, 2011.

Pitteway, M. L. V., and C. O. Hines, The Reflection and Ducting of Atmospheric Acoustic–Gravity Waves, *Can. J. Phys.*, *43*(12), 2222–2243, doi:10.1139/p65-217, 1965.

Press, W. H., *Numerical Recipes in C: The Art of Scientific Computing*, Cambridge University Press, 1992.

Rapp, M., and F.-J. Lübken, Polar mesosphere summer echoes (PMSE): Review of observations and current understanding, *Atmos. Chem. Phys.*, *4*, 2601–2633, 2004.

Rapp, M., and G. E. Thomas, Modeling the microphysics of mesospheric ice particles: Assessment of current capabilities and basic sensitivities, *J. Atmos. Solar-Terr. Phys.*, *68*(7), 715–744, doi:http://dx.doi.org/10.1016/j.jastp.2005.10.015, 2006.

Rapp, M., F.-J. Lübken, A. Müllemann, G. E. Thomas, and E. J. Jensen, Small-scale temperature variations in the vicinity of NLC: Experimental and model results, *J. Geophys. Res.*, *107*(D19), AAC 11–1–AAC 11–20, doi:10.1029/2001JD001241, 2002.

Rusch, D. W., G. E. Thomas, W. McClintock, A. W. Merkel, S. M. Bailey, J. M. Russell III, C. E. Randall, C. Jeppesen, and M. Callan, The cloud imaging and particle size experiment on the aeronomy of ice in the mesosphere mission: Cloud morphology for the northern 2007 season, *J. Atmos. Solar-Terr. Phys.*, *71*(3–4), 356–364, doi:http://dx.doi.org/10.1016/j.jastp.2008.11.005, 2009.

Russell, J. M., III, S. M. Bailey, L. L. Gordley, D. W. Rusch, M. Horányi, M. E. Hervig, G. E. Thomas, C. E. Randall, D. E. Siskind, M. H. Stevens, M. E. Summers, M. J. Taylor, C. R.

Englert, P. J. Espy, W. E. McClintock, and A. W. Merkel, The Aeronomy of Ice in the Mesosphere (AIM) mission: Overview and early science results, *J. Atmos. Solar-Terr. Phys.*, *71*(3–4), 289 – 299, doi:http://dx.doi.org/10.1016/j.jastp.2008.08.011, global Perspectives on the Aeronomy of the Summer Mesopause Region Eighth International Workshop on Layered Phenomena in the Mesopause Region, 2009.

Scargle, J. D., Studies in astronomical time series analysis. II - Statistical aspects of spectral analysis of unevenly spaced data, *Astrophys. J.*, *263*, 835–853, doi:10.1086/160554, 1982.

Simkhada, D. B., J. B. Snively, M. J. Taylor, and S. J. Franke, Analysis and modeling of ducted and evanescent gravity waves observed in the Hawaiian airglow, *Ann. Geophys.*, *27*(8), 3213–3224, doi:10.5194/angeo-27-3213-2009, 2009.

Singer, W., R. Latteck, and D. A. Holdsworth, A new narrow beam Doppler Radar at 3 MHz for studies of the high-latitude middle atmosphere, *Adv. Space Res.*, *41*, 1487–1493, doi:10.1016/j.asr.2007.10.006, 2008.

Stroud, W. G., W. Nordberg, W. R. Bandeen, F. L. Bartman, and P. Titus, Rocket-grenade measurements of temperatures and winds in the mesosphere over Churchill, Canada, *J. Geophys. Res.*, *65*(8), 2307–2323, doi:10.1029/JZ065i008p02307, 1960.

Taylor, M., P.-D. Pautet, Y. Zhao, C. Randall, J. Lumpe, S. Bailey, J. Carstens, K. Nielsen, J. M. Russell III, and J. Stegman, High-Latitude Gravity Wave Measurements in Noctilucent Clouds and Polar Mesospheric Clouds, in *Aeronomy of the Earth's Atmosphere and Ionosphere*, *IAGA Special Sopron Book Series*, vol. 2, edited by M. A. Abdu and D. Pancheva, pp. 93–105, Springer Netherlands, doi:10.1007/978-94-007-0326-1_7, 2011.

Taylor, M. J., W. R. Pendleton, S. Clark, H. Takahashi, D. Gobbi, and R. A. Goldberg, Image measurements of short-period gravity waves at equatorial latitudes, *J. Geophys. Res.*, *102*(D22), 26,283–26,299, doi:10.1029/96JD03515, 1997.

Thayer, J., M. Rapp, A. Gerrard, E. Gudmundsson, and T. Kane, Gravity wave influences on Arctic mesospheric clouds as determined by a Rayleigh lidar at Sondrestrom, Greenland, *J. Geophys. Res.*, *108*(D8), 8449, doi:10.1029/2002JD002363, 2003.

Thomas, G. E., Is the polar mesosphere the miner's canary of global change?, *Adv. Space Res.*, *18*(3), 149–158, doi:http://dx.doi.org/10.1016/0273-1177(95)00855-9, 1996.

Thomas, G. E., J. J. Olivero, M. DeLand, and E. P. Shettle, A response to the article by U. von Zahn, "Are noctilucent clouds truly a "miner's canary" for global change ?", *Trans. Am. Geophys. Union (EOS)*, *84*(36), 352–553, doi:10.1029/2003EO360008, 2003.

von Cossart, G., J. Fiedler, and U. von Zahn, Size distributions of NLC particles as determined from 3-color observations of NLC by ground-based lidar, *Geophys. Res. Lett.*, *26*(11), 1513–1516, doi:10.1029/1999GL900226, 1999.

von Zahn, U., Are noctilucent clouds truly a "Miner's Canary" for global change?, *Trans. Am. Geophys. Union (EOS)*, *84*(28), 261–264, doi:10.1029/2003EO280001, 2003.

von Zahn, U., G. von Cossart, J. Fiedler, and D. Rees, Tidal variations of noctilucent clouds measured at 69°N latitude by groundbased lidar, *Geophys. Res. Lett.*, *25*(9), 1289–1292, doi:10.1029/98GL00546, 1998.

von Zahn, U., G. von Cossart, J. Fiedler, K. H. Fricke, G. Nelke, G. Baumgarten, D. Rees, A. Hauchecorne, and K. Adolfsen, The ALOMAR Rayleigh/Mie/Raman lidar: objectives, configuration, and performance, *Ann. Geophys.*, *18*(7), 815–833, doi:10.1007/s00585-000-0815-2, 2000.

Walterscheid, R., J. Hecht, R. Vincent, I. Reid, J. Woithe, and M. Hickey, Analysis and interpretation of airglow and radar observations of quasi-monochromatic gravity waves in the upper mesosphere and lower thermosphere over Adelaide, Australia (35°S, 138°E), *J. Atmos. Solar-Terr. Phys.*, *61*(6), 461 – 478, doi:http://dx.doi.org/10.1016/S1364-6826(99)00002-4, 1999.

Wandinger, U., Introduction to Lidar, in *Lidar*, *Springer Series in Optical Sciences*, vol. 102, edited by C. Weitkamp, pp. 1–18, Springer New York, doi:10.1007/0-387-25101-4_1, 2005.

Wegener, A., Die Erforschung der obersten Atmosphärenschichten, *Gerl. Beitr. Geophys.*, *11*, 104–124, 1912.

Wilms, H., M. Rapp, P. Hoffmann, J. Fiedler, and G. Baumgarten, Gravity wave influence on NLC: experimental results from ALOMAR, 69° N, *Atmos. Chem. Phys.*, *13*(23), 11,951–11,963, doi:10.5194/acp-13-11951-2013, 2013.

Witt, G., Height, structure and displacements of noctilucent clouds, *Tellus*, *14*(1), 1–18, doi:10.1111/j.2153-3490.1962.tb00115.x, 1962.

Witt, G., Optical characteristics of mesospheric aerosol distributions in relation to noctilucent clouds, *Tellus*, *20*(1), 98–114, 1968.

Acknowledgements

In a first place, I would like to thank Prof. Dr. Franz-Josef Lübken, for offering me the possibility to do my Master at the IAP.
For his advice, many ideas, and help, as well as the organisation of my two stays at the ALOMAR observatory, I would like to thank Dr. Gerd Baumgarten. He and Dr. Jens Fiedler made this thesis possible by their ideas and guidance. For his detailed corrections and support, until the last page was printed, I thank Dr. Jens Hildebrand. The radar data used in the thesis was provided by Dr. Irina Strelnikova.

Furthermore, I would like to thank all those who made the time in the institute, on the way to the institute (which should not be underestimated) and in Norway, especially the Norwegian ALOMAR staff, a pleasant and interesting time. In particular, Francie, Jens and Lasse made the time at the office always enjoyable.
I would like to thank my family for their support, particularly in the last days.

Selbständigkeitserklärung

Ich versichere hiermit an Eides statt, dass ich die vorliegende Arbeit selbständig angefertigt und ohne fremde Hilfe verfasst habe, keine außer den von mir angegebenen Hilfsmitteln und Quellen verwendet habe und die den benutzten Werken inhaltlich und wörtlich entnommen Stellen als solche kenntlich gemacht habe.

Rostock, den 12. September 2014